Journal of Nanobiotechnology

RESEARCH Open Access

Protective effects of bone marrow mesenchymal stem cell-derived exosomes loaded cerium dioxide nanoparticle against deoxynivalenol-induced liver damage

Zitong Meng[1,2,3,4], Mingmeng Tang[1,3,4], Shiyin Xu[1,3,4], Xiaolei Zhou[1,3,4], Zixuan Zhang[1,3,4], Liunan Yang[1,3,4], Andreas K. Nüssler[5], Liegang Liu[1,3,4] and Wei Yang[1,3,4*]

Abstract

Background Deoxynivalenol (DON), a mycotoxin produced by Fusarium species, posed significant threats to food safety and human health due to its widespread prevalence and detrimental effects. Upon exposure, the liver, which played a crucial role in detoxifying DON, experienced depleted antioxidant levels and heightened inflammatory responses. Bone marrow mesenchymal stem cell (BMSC)-derived exosomes (BMSC-exos) exhibited therapeutic potential by promoting cellular repair and delivering bioactive substances, such as cerium dioxide nanoparticles (CeO_2 NPs), which are recognized for their ability to mitigate oxidative stress and inflammation.

Results We successfully loaded BMSC-exos with CeO_2 NPs (BMSC-exos @ CeO_2) using extrusion techniques, verified through electron microscopy and elemental mapping. The resulting BMSC-exos @ CeO_2 displayed low cytotoxicity, boosted antioxidant activity, and reduced inflammation in Hepa 1–6 cells with DON condition. In vivo study, BMSC-exos @ CeO_2 maintained stability for 72 h, it also can prevent antioxidant depletion and inhibit liver inflammation under the DON condition. After BMSC-exos @ CeO_2 treatment, multi-omics analyses further highlighted significant changes in metabolic and protein signaling pathways, notably in linoleic and arachidonic acid metabolism. Key pathways about AMPK and JAK1/STAT3 were involved in mitigating liver damage with or without DON.

Conclusion Our findings revealed BMSC-exos @ CeO_2 as a promising therapeutic strategy against DON's toxicity, offering valuable insights into their potential for liver protection.

*Correspondence:
Wei Yang
yw8278@hotmail.com; yw8278@hust.edu.cn

Full list of author information is available at the end of the article

Graphical abstract

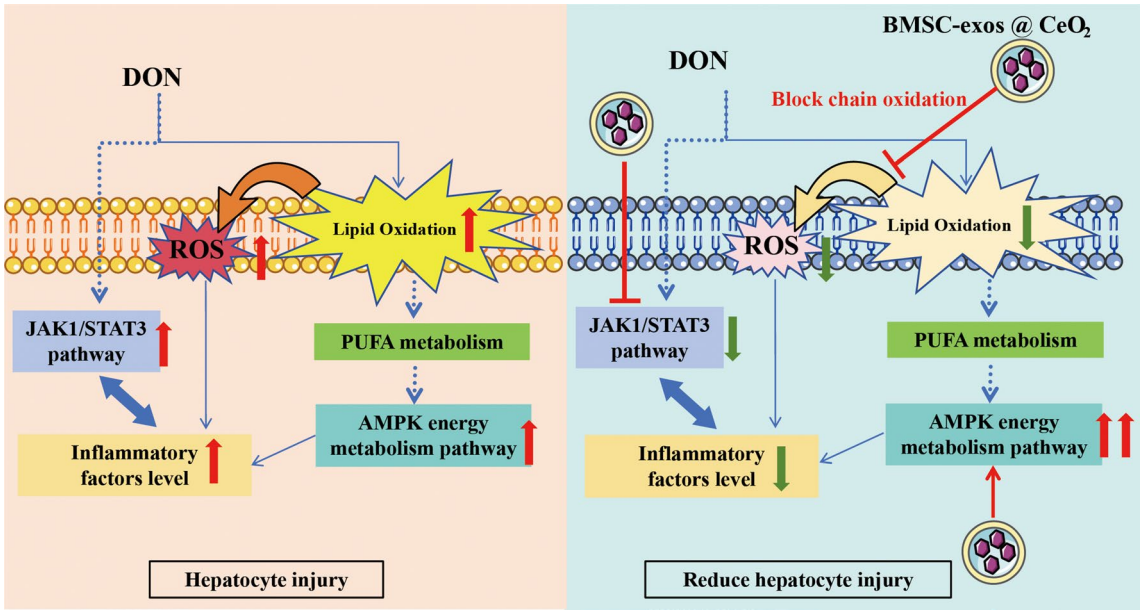

Keywords Deoxynivalenol, BMSC-exos @ CeO_2, Oxidative stress, Inflammation, Hepatic damage

Introduction

Deoxynivalenol (DON), a mycotoxin commonly found in grains and grain-based products, posed significant health risks to humans and animals upon exposure [1, 2]. Different levels of DON contamination in food and feed led to adverse health effects, such as vomiting in pigs and disrupting immune responses and liver function in mice [3, 4]. Epidemiological studies also suggested potential risks to human health from both acute and chronic DON exposure [5]. A recent cohort study showed that long-term, low-level exposure to DON could disrupt growth hormone expression in pregnant women, which was primarily produced by the liver [6], potentially leading to decreased fetal birth weight and length, and an increased risk of small-for-gestational-age (SGA) births [7, 8].

DON induced oxidative stress, an early pathological event that led to organ damage, by promoting the dose-dependent production of reactive oxygen species (ROS) [9, 10]. This oxidative damage was associated with DON's chemical structure, which included reactive hydroxyl groups [11]. In previous studies, DON was shown to increase ROS levels, impacting AMP-activated protein kinase (AMPK) expression and thereby inhibiting autophagy in grass carp liver cells (L8824) [12]. DON also induced inflammation, which decreased AMPK protein expression and reduced glucose absorption in IPEC-J2 cells [13]. Additionally, DON-mediated intestinal damage was linked to alterations in the expression of interleukins IL-1β and IL-6 as well as the Janus kinase/signal transducer and activator of transcription (JAK/STAT) signaling pathway [14–16]. Our previous studies observed similar molecular mechanisms and phenotypic effects in the liver and colon [17–22]. Therefore, targeting the inhibition or reduction of DON-induced oxidative stress and inflammation was a primary therapeutic objective. Despite advancements in understanding the harmful and toxic effects of DON, effective strategies for mitigating these adverse effects remain lacking. This underscores a significant research gap, which our study aims to address by investigating the potential of advanced nanomaterials and exosomal delivery systems to counteract DON-induced oxidative stress and inflammation.

Mesenchymal stem cell (MSC)-derived exosomes (MSC-exos) gained recognition as a promising therapeutic strategy in both research and clinical applications [23, 24]. Our previous studies indicated that BMSC-exos could interact with free radicals, as polyunsaturated fatty acids (PUFAs) within their lipid bilayers served as primary targets for ROS attack [25, 26]. This highlighted the potential of BMSC-exos in interrupting the lipid peroxidation chain reaction—a key process in oxidative damage to cellular membranes [22]. Additionally, we focued on CeO_2 NPs as innovative antioxidant agents. CeO_2 NPs acted as scavengers for ROS and reactive nitrogen species and exhibited enzyme-mimetic activities similar to superoxide dismutase (SOD), catalase (CAT), and glutathione peroxidase (GSH-Px) [27–29]. Uniquely, CeO_2 NPs could switch between Ce^{3+} and Ce^{4+} oxidation states

($Ce^{3+} \rightleftharpoons Ce^{4+}$), allowing it to sustain antioxidant activity without depletion [30].

Notably, studies showed that MSC-exos loaded with CeO_2 nanocrystals (MSCExo-Ce or BMSC-exos @ CeO_2) effectively reduced ROS and inflammation levels, while also demonstrating good biocompatibility in treating conditions such as dry eye syndrome (DES) [31]. Furthermore, Ce-loaded macrophage exosomes were shown to modulate the immune microenvironment and repair endothelial damage [32]. Another study also indicated that nanoceria exerted potent antioxidant and anti-inflammatory effects in hepatocellular carcinoma [33]. Recent studies highlighted the potential advancements of various nanomaterials. For instance, Hyaluronic acid/gelatin (HA/GEL) scaffolds encapsulated with metformin-loaded mesoporous silica nanoparticles (MET @ MSNs) were shown to enhance the proliferation of bone marrow-derived human mesenchymal stem cells (BM-hMSCs) without accelerating cellular aging [34]. Chitosan nanofiber dressings containing cerium oxide nanoparticles (CeO_2-CSNPs) synthesized with Thymus vulgaris extract exhibited significant antimicrobial and antioxidant properties, promoting diabetic wound healing [35]. MSC demonstrated potential therapeutic benefits in conditions related to COVID-19 [36]. At the same time, dual-stage curcumin release from electrospun polycaprolactone/gelatin (PCL/GEL) nanofibers supported the proliferation and longevity of adipose-derived stem cells (hADSCs) [37]. Additionally, ZSM-5 zeolite/polycaprolactone-polyethylene glycol (PCL-PEG) nanofibers facilitated the sustained release of dexamethasone (DEX) and ascorbic acid (ASC), promoting osteogenic differentiation [38]. Despite existing challenges, nanotechnology was promising for targeted liver disease therapy [39]. However, the protective effects of BMSC-exos @ CeO_2 against DON-induced liver damage remained unclear. By drawing on recent research regarding the potential of novel nanomaterials in therapeutic applications [39, 40], our study also highlighted its innovative approach and situated itself within the broader context of this field, emphasizing its significance. Given the loading capacity of BMSC-exos, we proposed encapsulating CeO_2 NPs within BMSC-exos (BMSC-exos @ CeO_2) to counteract and/or reduce inflammatory responses and enhance antioxidant activity under DON exposure. We will also employed multi-omics platforms and associated analytical methods to explore/decipher/identify the molecular mechanisms by which BMSC-exos @ CeO_2 mitigated DON-induced liver injury in C57BL/6J mice. This study addressed a significant research gap and aimed to provide new insights and a potential therapeutic approach for preventing and treating DON-induced organ damage, with implications for improving food safety and public health.

Materials and methods

Reagents

DON was purchased from Pribolab Biotech Co., Ltd. (Qingdao, China). Phosphatase and protease inhibitors were obtained from Bimake (Houston, USA). Fetal bovine serum (FBS) and DMEM/F12 medium were acquired from Thermo Fisher Scientific (Waltham, USA). Exosome-depleted FBS was obtained from System Biosciences (California, USA). The Total Glutathione Peroxidase (GPx, S0058), CAT (S0051), Total SOD (S0101), DAPI, Hoechst 33,342, and Edu-555 Cell Proliferation Assay Kits were purchased by Beyotime Institute of Biotechnology (Shanghai, China). PKH26 dye was purchased from Sigma-Aldrich (St. Louis, MI, USA), and Cyclosporin A dye was acquired from Yisheng Biotech Co., Ltd. (Shanghai, China). The Cell Proliferation and Cytotoxicity Assay Kit (CCK-8) was purchased from Dojindo Science Technology Inc. (Tokyo, Japan). Additionally, the Hydroxyl Radical Scavenging and Superoxide Anion Scavenging Assay Kits were obtained from Solarbio Life Sciences Co., Ltd. (Beijing, China).

Preparation and characterization of BMSC-exos @ CeO_2

Isolation and purification of BMSC-exos

In this study, the isolation and purification of BMSC-exos accorded to our previous publication [22] and the MISEV2023 guidelines established by the International Society for Extracellular Vesicles (ISEV) [41]. Specifically, BMSC were isolated from the femoral bone marrow of 50 male SPF-grade SD rats (3 weeks old, weighing 60–90 g, supplied by Beijing Vital River Laboratory Animal Technology Co., Ltd.) [22]. Exosomes were extracted from BMSCs at passages 3 to 5 using ultracentrifugation. Upon reaching 80% confluence, the cells were washed with phosphate-buffered saline (PBS) and incubated in DMEM/F12 medium supplemented with exosome-depleted fetal bovine serum (FBS) for 48 h. The collected cell supernatant underwent differential centrifugation at 4 °C utilizing an SW41Ti rotor and Optima XE-100 ultracentrifuge (Beckman Coulter, USA). This process involved sequential centrifugation: first at 300×g for 10 min, then 2000×g for another 10 min, and then at 10,000×g for 30 min to eliminate cellular debris. Finally, high-speed centrifugation was performed at 100,000×g for 70 min to discard the supernatant. The pellet was washed with PBS and resuspended. Subsequently, another round of centrifugation at 100,000×g for an additional 70 min was conducted to remove any remaining supernatant, thereby isolating and purifying BMSC-exos. The final suspension of BMSC-exos was resuspended in PBS and filtered through a sterile membrane filter with a pore size of 0.22 μm. Protein quantification was performed before the immediate packaging of BMSC-exos for subsequent applications.

Packaging or encapsulating process and methods of BMSC-exos @ CeO_2

This method was accorded to the previous study [42]. The CeO_2 NPs were obtained from Sigma-Aldrich, exhibiting a particle size of less than 25 nm in diameter (Item No. 544841, St. Louis, MI, USA). The CeO_2 NPs were suspended in PBS at a concentration of 5 mg/mL and subjected to sonication using a sonicator set at 100% amplitude, comprising cycles of 10 s of sonication followed by 10 s of pause, repeated for a total duration of 10 min-to achieve a homogeneous suspension.

Regarding to encapsulation of CeO_2 NPs with BMSC-exos, a weight ratio of 1:20 (w/w) was employed, mixing BMSC-exos (5 mg protein content) with CeO_2 NPs (0.25 mg) [22, 43]. The mixture was extruded through a polycarbonate porous membrane with a pore size of 200 nm using an Avantimini extruder (Item No. 610000, Avanti Polar Lipids, Alabama, US) within a biosafety cabinet, undergoing extrusion for fifteen cycles [42, 44]. Packaged BMSC-exos @ CeO_2 were collected after elution through the membrane. Before extrusion, the Avantimini extruder was sterilized by UV irradiation for 30 min to ensure aseptic conditions. During the concrete process, samples were injected from one side while collected on the opposite side to maintain sterility throughout handling.

Morphology of BMSC-exos @ CeO_2 and biomarkers of BMSC-exos

This section also referred to previous studies with the following experiments [31, 32, 42].

The Zeta potential of BMSC-exos particles and BMSC-exos @ CeO_2 was measured using a Malvern Zetasizer Nano ZS90. Samples were placed in DTS10701 cuvettes and analyzed under the following conditions: water as the dispersant, temperature set to 25 °C, equilibration time of 120 s, measurement duration ranging from a minimum of 10 runs to a maximum of 100 runs, with three replicate measurements.

The scattering light signals of BMSC-exos particles and BMSC-exos @ CeO_2 were detected using nanoparticle tracking analysis (NTA) technology (NanoSight NS300, Malvern, UK). Three 60-second videos were recorded for each sample at 30 frames per second. The hydrodynamic radius and concentration of the particles were calculated using NTA 3.3 Dev Build 3.3.104 software by tracking their Brownian motion. The experimental setup included an sCMOS camera with a Blue 488 nm laser, camera brightness level set to 10, rolling shutter value of 696, gain value of 73, and frame rate of 25.0 FPS. A total of 1498 frames were captured. The experimental temperature was maintained at 25 °C, viscosity was 1.0 cP, and samples were diluted 1×10^3-fold. The injection pump speed was set to 75 μL/min. During data analysis, the detection threshold was set to 2, blur size and maximum jump distance were set to automatic (ranging from 11.9 to 12.2 pixels).

The morphology of BMSC-exos @ CeO_2 was characterized using scanning electron microscopy (SEM, ZEISS Gemini 300, Germany) and transmission electron microscopy (TEM, JEOL-2100, Japan). The elemental distribution was analyzed by Smartedx (Carl Zeiss, Germany) and JED-2300T (JEOL, Japan) [45]. Initially, the sample was dispersed onto silicon wafers and subjected to gold sputtering for 45 s at a current of 10 mA using a sputter coater (SC7620, Oxford Quorum, UK). The morphological features were subsequently imaged with a Zeiss Sigma 300 scanning electron microscope (Carl Zeiss, Germany) at an accelerating voltage of 3 kV for morphology imaging and 15 kV for energy-dispersive X-ray spectroscopy (EDS) mapping, utilizing an SE2 secondary electron detector (Carl Zeiss, Germany). Additionally, the sample was also placed on copper grids to dry before conducting morphology assessment and EDS mapping using a JEM-F200 (JEOL, Japan) at an accelerating voltage of 200 kV in conjunction with the JED-2300T EDS system (JEOL, Japan).

To detect the protein markers CD9, CD81, and TSG101 of BMSC-exos [22, 46], the 20 μg of protein was separated using a 12% SDS-PAGE gel and subsequently transferred to a 0.45 μm nitrocellulose membrane (Millipore, USA). Following blocking with 5% non-fat milk in T-BST, the membrane was incubated overnight at 4 °C with primary antibodies against CD9 (ab223052), CD81 (ab109201), and TSG101 (ab133586) obtained from Abcam (Cambridge, UK), all diluted to a ratio of 1:1000. After 1 h incubation with a horseradish peroxidase-conjugated secondary antibody (#7076, 1:10000, Cell Signaling Technology, MA, USA), proteins were visualized using an enhanced chemiluminescence (ECL) substrate (Beyotime, Shanghai, China). The images were analyzed utilizing GeneSnap and GeneTools software (Syngene, UK).

Cell lines and treatments

Cell grouping and treatment

In this section, the dose of DON and intervention time were based on our previous studies [18]. The mouse hepatocellular carcinoma cell line Hepa 1–6 (CRL-1830™) was obtained from the American Type Culture Collection (ATCC, Manassas, VA, USA). Hepa 1–6 cells (2×10^6 cells per well) were divided into five groups, with each group cultured in three parallel wells: **(1)** Control group: Hepa 1–6 cells + PBS (0.01 M) for 24 h. **(2)** DON group: Hepa 1–6 cells + 0.6 μM DON for 24 h. **(3)** DON + BMSC-exo group: Hepa 1–6 cells + 0.6 μM DON + 0.4 mg/mL BMSC-exos for 24 h. **(4)** DON + CeO_2 NPs group: Hepa 1–6 cells + 0.6 μM DON + 20 μg/mL CeO_2 for 24 h [47,

48]. **(5)** DON + BMSC-exos @ CeO_2 group: Hepa 1–6 cells + 0.6 μM DON + BMSC-exos @ CeO_2 (CeO_2 NPs concentration also referred to the result of CCK8) for 24 h. After treatment, the cells were collected for subsequent experiments.

Observation for uptake of BMSC-exos @ CeO_2 by Hepa 1–6 cells

BMSC-exos @ CeO_2 were labeled by the PKH26 dye, followed by centrifugation at 120,000×g for 90 min to remove excess dye, and then co-cultured with Hepa 1–6 cells. The cytoskeleton was also stained with FITC-labeled phalloidin and the nuclei were finally stained with DAPI, the image acquisition used by confocal microscope (FV3000, OMTOOLS, China).

Cell viability

The effect of BMSC-exos @ CeO_2 and CeO_2 NPs on the viability of Hepa 1–6 cells was evaluated using the CCK-8 kit. Cells were seeded in 96-well plates and incubated after adding different concentrations of reagents. Absorbance was determined using a microplate reader to assess cell viability.

Besides, the EdU staining assay was used to examine the effects of different treatments on the proliferation ability of Hepa 1–6 cells with or without DON. The quantification of cell proliferation was evaluated using fluorescence microscopy and Image J.

Measurement of antioxidant activity and free radicals scavenging

The hydroxyl radical and superoxide anion scavenging, antioxidants activities (SOD, Gpx and CAT), as well as intracellular superoxide anion levels in cells and tissues, were assessed according to the instructions (Solebao, Beijing, China).

Measurement levels of inflammation factor

Multi-index flow cytometric analysis (Abclonal, Wuhan, China) was conducted with specific antibodies covalently linked to encoded microspheres to quantitatively detect various inflammatory cytokines in different samples (cells and liver tissue) [49]. The data recorded (TNF-α, IL-1β, IL-2, IL-4, IL-6, IL-12, Il-17 A and INF-γ) by flow cytometric analyzer (ABplex-100, Abclonal, China).

Animal care, treatments, and study design

Animals' housing and treatments

All procedures in this animal experiment have been approved by the Institutional Animal Care and Use Committee of Huazhong University of Science and Technology (IACUC number: 3622).

The 8-week-old SPF-grade male C57BL/6J mice (Total 30 mice), weighing between 16 g and 22 g, were purchased from Beijing Vital River Laboratory Animal Technology Co., Ltd. and housed in the SPF animal laboratory at the Pesticide Toxicology Research Center of Tongji Medical College, Huazhong University of Science and Technology.

The environmental temperature was controlled at 22 °C ± 2 °C, with 60% humidity and a 12 h light/dark cycle (8:00 AM to 8:00 PM), with food and water available *ad libitum*. The bedding and drinking water were changed twice a week. All animal housing and experimental processes adhered strictly to the "Regulations on the Administration of Laboratory Animals in China".

Experiment design

Thirty mice were purchased and housed in an SPF-level animal facility. After a one-week acclimatization period, each mouse was ear-tagged and randomly assigned to one of three groups ($N = 10$ per group): control group, DON group, and DON + BMSC-exos @ CeO_2 group.

Mice in the DON group and the DON + BMSC-exos @ CeO_2 group received DON via oral gavage twice weekly at a dose of 4 mg/kg body weight (BW) [50]. Mice in the DON + BMSC-exos @ CeO_2 group also received intravenous injections of BMSC-exos @ CeO_2 via the tail vein, twice weekly for 14 days [33, 51]. The BMSC-exos @ CeO_2 were prepared at a ratio of 20:1 (w/w) based on BMSC-exos (5 mg, protein content) and CeO_2 NPs (0.25 mg). The intravenous dose of BMSC-exos was 4 mg/kg BW, and the dose of CeO_2 NPs was 200 μg/kg BW [22, 43, 51].

Mice in the control group received ultrapure water via oral gavage and PBS via tail vein injection, matching the volume and frequency of treatments administered to the other groups.

Tracing distribution of BMSC-exos @ CeO_2 in mice

Small animal live imaging

The live optical imaging methodology of small animal was adapted from previously published studies [22].

BMSC-exos @ CeO_2 were stained with DiR dye by incubating at 37 °C in the dark for 30 min, and then centrifuged to remove the supernatant and resuspended in PBS.

After tail vein injections, live bioluminescence imaging of the mice was captured using a small animal optical imaging system (Lago X optical imaging systems; SI Imaging, USA) at excitation/emission wavelengths of 745 nm/770 nm within 0 to 72 h, the luminescence from various organs was observed, recorded and calculated by software (Spectral Instruments Imaging, LLC 420 N. Bonita Avenue, Tucson, AZ 85745 USA).

Inductively coupled plasma spectrometer (ICP-MS) measures for Ce contents in liver

In this section, Ce concentrations in the liver were quantified using ICP-MS (Agilent 7800, California, USA) at 24, 48, and 72 h following the administration of BMSC-exos @ CeO_2 and CeO_2 NPs, respectively [33, 51]. Initially, samples were accurately weighed and placed into crucibles pre-treated with nitric acid for digestion at 120 °C by microwave-assisted methods. After cooling, the digested solutions were diluted to a predetermined volume with deionized water. Standard solutions across various concentration gradients were prepared to establish a calibration curve. During ICP-MS analysis, samples were appropriately diluted to ensure they remained within the calibration range. Final results were reported in micrograms per kilogram (μg/kg). The analytical parameters were configured as follows: pump rate set at 20 r/min, nebulizer flow maintained at 1.00 L/min, auxiliary gas flow at 1.00 L/min, sample flush time of 40 s, and radiofrequency power adjusted to 1550 W.

4D-DIA quantitative proteomics of mouse liver

Quantitative proteomics of mouse liver after treatment referred to previous studies [52–55].

Sample Preparation and detection

Samples were ground in liquid nitrogen, lysed with buffer, and ultra-sonicated. Supernatants were collected by centrifugation and quantified. After proteolysis and desaltation, samples were precipitated with acetone and resuspended in ammonium bicarbonate solution for overnight digestion. Desalted with a C18 column, then re-dissolved and separated using the NanoElute UHPLC system. Solvent A was 0.1% formic acid aqueous solution, and B was 0.1% formic acid acetonitrile solution. The separated samples were analyzed using a timsTOF Pro2 mass spectrometer in ddaPASEF and diaPASEF modes.

Mass spectrometry data analysis and protein quantification

DIA mass spectrometry data was searched using DIA-NN software, leveraging deep learning to predict spectral libraries, and MBR-generated libraries were reanalyzed. The FDR for precursor ions and protein levels was set at 1%. Quantitative data was normalized by centering transformation, with differential analysis using t-tests or ANOVA.

Bioinformatics analysis

Comprehensive functional annotation of identified and differential proteins was performed to reveal expression changes and related physiological functions across groups, including GO, KOG, KEGG pathway, protein domain, subcellular localization, and signal peptide analyses. Differential proteins were subjected to GO classification, KOG functional classification, KEGG pathway, protein domain enrichment analysis, subcellular location, and signal peptide predictions.

Non-targeted metabolomics for mouse liver

The non-targeted metabolomics analysis of mouse liver after treatment referred to previous studies [56, 57].

Sample Preparation and extraction

Twenty micrograms of liver samples were placed in numbered centrifuge tubes with beads and homogenized. After centrifugation, 400 μL of internal standard extraction solution was added, followed by shaking and standing. Centrifuge at 12,000 rpm for 10 min, transfer the supernatant to a new tube, allow it to stand in a refrigerator, then centrifuge again and collect the supernatant in a sample vial for further analysis.

Chromatographic column selection and mobile phase conditions

The LC/MS positive and negative ion detection modes were adopted. In the positive ion mode, a T3 chromatographic column was used with 0.1% formic acid water and 0.1% formic acid acetonitrile as solvents A and B. Gradient elution: From 5% B to 20% B within 2 min, to 60% B in 3 min, to 99% B in 1 min, maintained for 1.5 min then quickly returned to 5% B and maintained for 2.4 min. Negative ion mode used the same elution gradient. Column temperature was 40 °C, flow rate 0.4 mL/min, and injection volume was 4 μL.

Mass spectrometry conditions

The Analyst TF 1.7.1 software and AB TripleTOF 6600 mass spectrometer were used. In ESI + mode, the acquisition time was 10 min, ionization voltage 5000 V, ion source temperature 550 °C; in ESI- mode, the acquisition time was 10 min, ionization voltage – 4000 V, ion source temperature 450 °C. For MS1 and MS2, the mass range was set to 50-1000 Da, with acquisition times of 0.2 s and 0.04 s respectively.

Data analysis

Raw data was converted to mzXML format, peaks were extracted and retention time was corrected using the XCMS program. Peaks with high missing rates were filtered and filled, and peak areas were adjusted using the SVR method. Metabolite identification was performed through database searching and the metDNA method, selecting substances with high scores and low CV values. Subsequent analysis included principal component analysis (PCA), hierarchical clustering analysis, Pearson correlation coefficient calculation, differential metabolite selection (determined by VIP or/and P-value), and KEGG annotation and enrichment analysis.

Detection of Oxylipins and energy metabolites in mouse liver

Detection of Oxylipins

In this section, we referred to a previous publication [58]. Eicosanoids and their deuterated standards were bought from Cayman Chemical, while HPLC-grade solvents and acetic acid were obtained from Merck and Sigma-Aldrich, respectively. Samples were prepared by thawing at -80 °C, homogenizing with a methanol/acetonitrile solution containing an internal standard, and extracting proteins at -20 °C before centrifugation. The supernatant was then processed using Poly-Sery MAX SPE columns. For UPLC/MS/MS analysis, the samples were analyzed on a Waters ACQUITY UPLC HSS T3 C18 column with a water-acetonitrile gradient containing acetic acid. The QTRAP® 6500 + LC-MS/MS System with ESI in negative mode was used for detection, employing scheduled multiple reaction monitoring for eicosanoid analysis, with data acquisition and quantification managed by Analyst 1.6.3 and Multiquant 3.0.3 software, respectively.

Detection of energy metabolites

In this section, we referred to previous publications [59]. Samples were prepared by thawing, homogenizing, and extracting with 70% methanol. After vortexing and centrifugation, the supernatant was processed through a Protein Precipitation Plate for LC-MS. The UPLC analysis was performed on a Waters ACQUITY H-Class system with an amide column, using a water gradient with ammonium additives and acetonitrile. The flow rate was 0.4 mL/min at 40 °C, with a 2 μL injection volume. MS analysis utilized a QTRAP® 6500 + system with both positive and negative ESI. Parameters were optimized for each metabolite, and data were acquired and quantified using Sciex software. The method involved scheduled multiple reaction monitoring for targeted metabolite analysis.

Western blotting

Our experimental procedures were following previously published studies [60]. We employed primary antibodies against AMPKα (#5831, 1:1000, Cell Signaling Technology, MA, USA), p-AMPKα (Thr172) (#2535, 1:1000, Cell Signaling Technology, MA, USA), P-JAK1 (ab138005, 1:1000, Abcam, UK), JAK1 (ab133666, 1:1000, Abcam, UK), P-STAT3 (#9145, 1:1000; Cell Signaling Technology; MA; USA), STAT3 (#79D7; 1:1000; Cell Signaling Technology; MA; USA), and GAPDH (#5174; 1: 10,000; Cell Signaling Technology; MA; USA). Secondary HRP-linked antibodies (#7076; 1:10,000) were utilized alongside Lumigen ECL Ultra detection reagents (Lumigen Inc., MI, USA) for protein visualization.

Data analysis

Prism software (GraphPad 8.0) was used for data processing, statistical analysis, and graphing. All experimental results were expressed as mean ± standard deviation. All data were derived from more than three independent experiments. For comparisons among multiple groups, one-way analysis of variance (ANOVA) was used to assess differences in means between groups. Tukey's post hoc test (Tukey's HSD test) was employed to correct for multiple comparisons, a widely recognized method to control the risk of Type I error associated with multiple comparisons. All adjusted P values from multiple comparisons were reported. The significance level was set at $P < 0.05$, meaning that results were considered statistically significant when the P value was below 0.05. This significance level was consistently applied across all statistical analyses.

Results

Characterization of BMSC-exos, CeO_2 NPs and BMSC-exos @ CeO_2

Pictures from TEM and SEM revealed that CeO_2 NPs appeared as spherical particles and BMSC-exos exhibited a "cup-shaped" morphology. The profile of BMSC-exos @ CeO_2 displayed a similar bilayer membrane structure (Fig. 1a-b). Data and pictures from EDS confirmed that cerium (Ce) and oxygen (O) elements were concentrated in the core, whereas membrane-associated elements such as nitrogen (N) and phosphorus (P) were distributed peripherally (Fig. 1c-d).

Results of NTA indicated that the particle sizes of both BMSC-exos and BMSC-exos @ CeO_2 predominantly ranged from 70 to 300 nm, with mode sizes measured at 127.3 ± 1.4 nm for BMSC-exos and 141.0 ± 2.9 nm for BMSC-exos @ CeO_2, this result bore a resemblance to those published in previous studies [32, 61]. Although no significant changes in particle size were observed at the D10 and D90 positions, there was a notable increase in particle size within moderate ranges for BMSC-exos @ CeO_2, this may have been attributed to smaller BMSC-exos being less effective at encapsulating CeO_2 NPs while larger exosomes experienced compression during chromatography to approximately 200 nm, leading medium-sized exosomes to exhibit an increase upon encapsulation of CeO_2 NPs (Fig. 1f-g).

Besides, Zeta potential analysis demonstrated that following loading, the surface charge of the particles became more negative, changing from + 4.213 mV for pure CeO_2 NPs to -10.89 mV for BMSC-exos and further decreasing to -21.57 mV for the BMSC-exos @ CeO_2 (Fig. 1h), this increased negative charge was advantageous that could reduce nonspecific adsorption, enhance blood circulation, maintain tissue penetration, ultimately improve bioavailability [42].

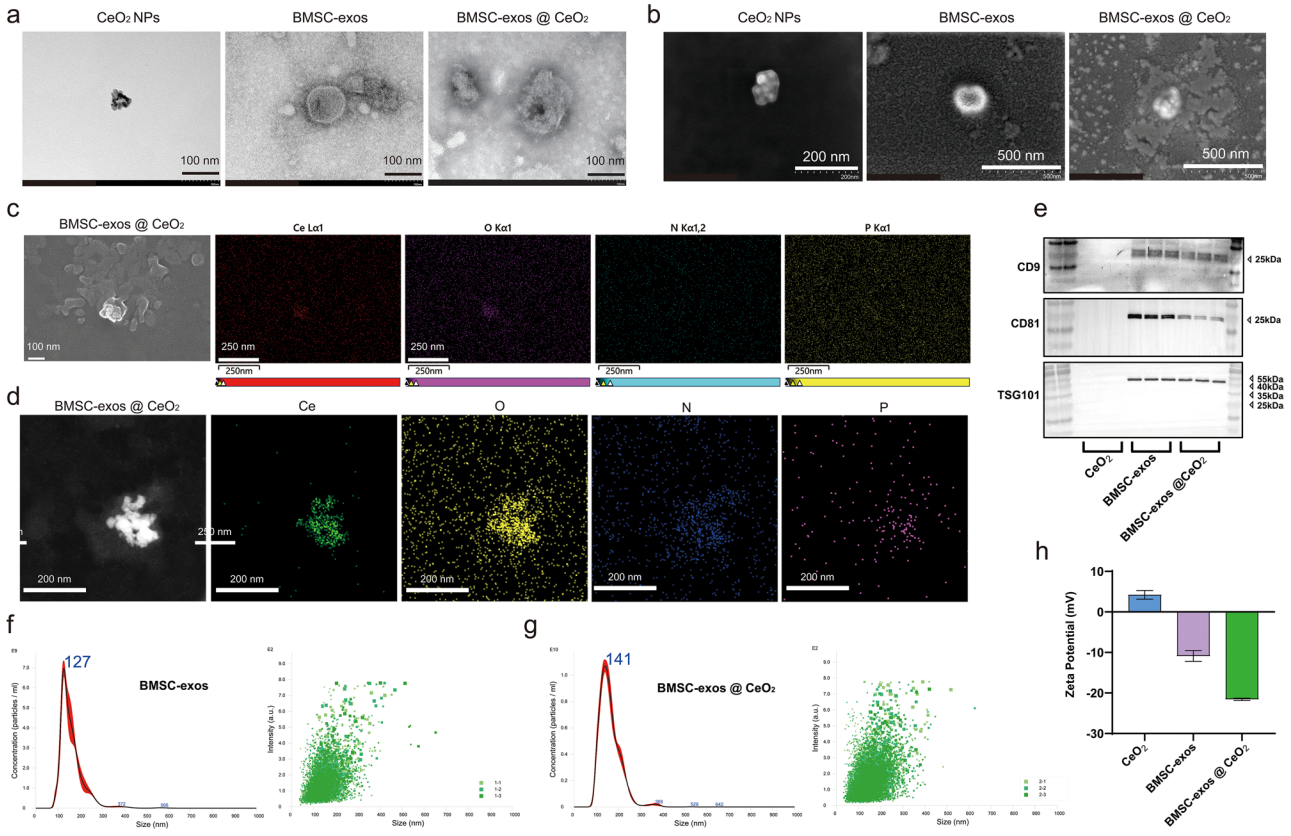

Fig. 1 Characterization of BMSC-exos @ CeO_2. (**a**) From left to right: images of CeO_2 NPs, BMSC-exos, and BMSC-exos @ CeO_2 were taken by TEM. Scale bar: 100 nm. (**b**) From left to right: images of CeO_2 NPs, BMSC-exos, and BMSC-exos @ CeO_2 were taken by SEM. Scale bars: 200 nm, 500 nm, and 500 nm, respectively. (**c**) EDS mapping of BMSC-exos @ CeO_2 by TEM. Scale bar: 250 nm. (**d**) EDS mapping of BMSC-exos @ CeO_2 by SEM. Scale bar: 250 nm. (**e**) Western blotting analysis for CD9, CD81 and TSG101 in CeO_2 NPs, BMSC-exos, and BMSC-exos @ CeO_2. (**f**-**g**) Particle size distribution of BMSC-exos and BMSC-exos @ CeO_2 were characterized by NTA. (**h**) Zeta potential of CeO_2 NPs, BMSC-exos, and BMSC-exos @ CeO_2

According to data from Western blotting, both BMSC-exos and BMSC-exos @ CeO_2 expressed exosome-specific markers CD9, CD81, and TSG101 (Fig. 1e), which could form "eat-me" signals between donor and recipient cells. This information also indicated that BMSC-exos @ CeO_2 met the exosome evaluation characteristics outlined in the newest guidelines (MISEV2023) by the International Society for Extracellular Vesicles (ISEV) [41]. These results also suggested that extrusion had not destroyed the membrane structure. However, these protein expressions were not detected on CeO_2 NPs (Fig. 1e).

Effects of BMSC-exos @ CeO_2 on cell viability, antioxidant activity, and anti-inflammatory responses under the DON condition

To investigate the protective effects of BMSC-exos @ CeO_2 on Hepa 1–6 cells treated with DON, we first confirmed the endocytosis of BMSC-exos @ CeO_2 by the cells. Following a co-culture for 3 h with PKH26-labeled BMSC-exos @ CeO_2, pictures revealed that fluorescent signaling was internalized and uniformly distributed in the cytoplasm of Hepa 1–6 cells (Fig. 2a).

Data from the EdU proliferation assay demonstrated that DON significantly inhibited cell proliferation. However, treatment of BMSC-exos @ CeO_2 effectively mitigated this inhibition and exhibited a trend compared to either BMSC-exos or CeO_2 NPs alone (Fig. 2b-c). The results of the CCK-8 assay indicated that at a concentration of 20 μg/mL, cell viability in both the CeO_2 NPs group and the BMSC-exos @ CeO_2 group exceeded 80%, demonstrating no significant difference in their effects on cell viability across concentrations ranging from 0 to 20 μg/mL (Fig. 2d). Notably, at a concentration of 40 μg/mL, cell viability was significantly highest in BMSC-exos @ CeO_2 group under the DON condition (Fig. 2d). Thus, a dosage of 20 μg/mL was selected for subsequent experiments.

Meanwhile, pictures of DHE staining revealed that superoxide anion levels were markedly elevated in DON group. Conversely, treatments involving CeO_2 NPs or BMSC-exos @ CeO_2 reduced superoxide anion levels (Fig. 2e-f). Furthermore, BMSC-exos @ CeO_2 group showed that substantially improved the scavenging capacity against levels of oxygen anions and hydroxyl

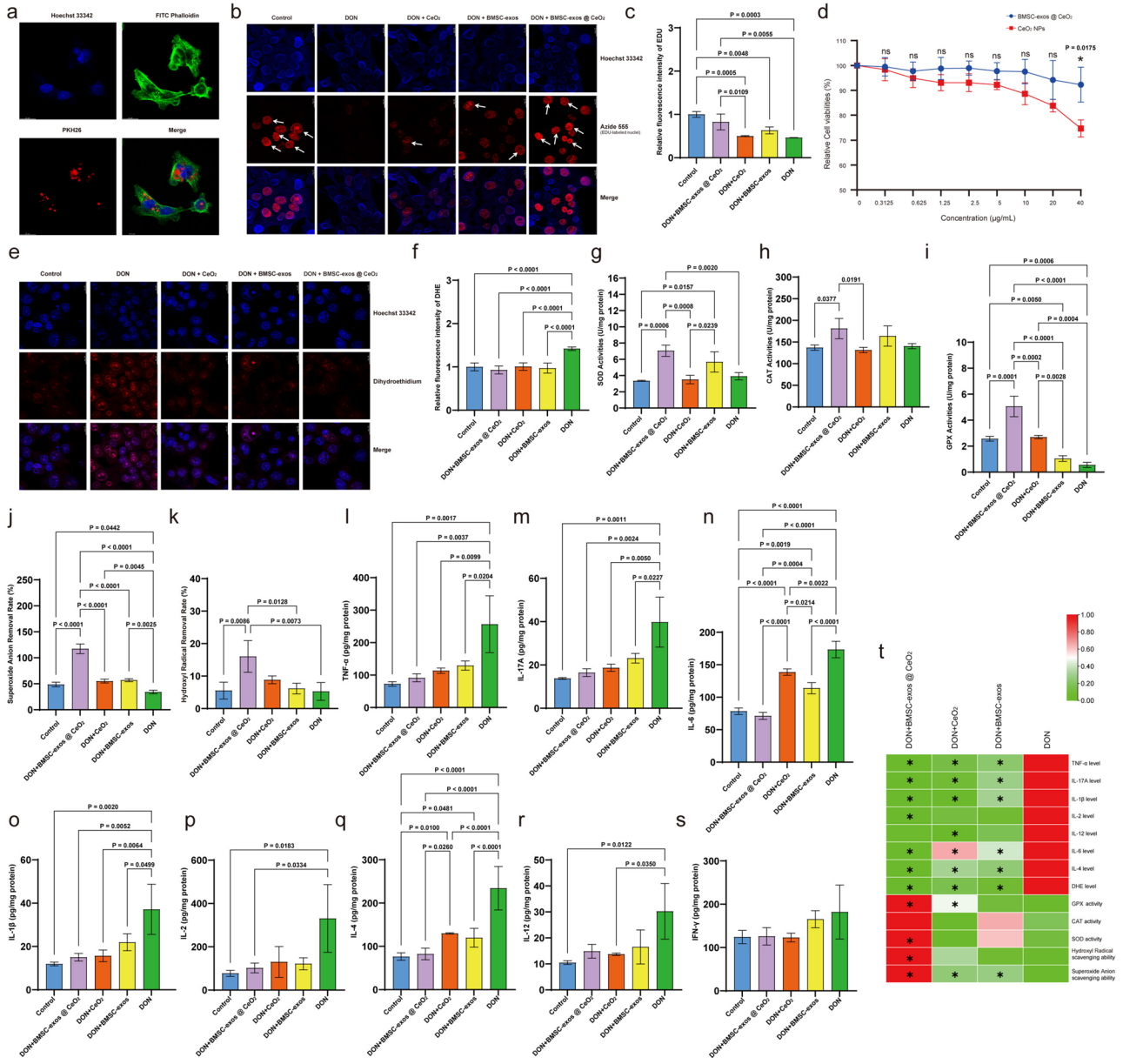

Fig. 2 Impact of BMSC-exos @ CeO_2 on cell viability, antioxidant activity, and anti-inflammatory responses in Hepa 1–6 cells under the DON treatment. (**a**) Uptake of BMSC-exos @ CeO_2: cell nuclei were stained with Hoechst 33,342 (blue), the cytoskeleton with FITC-phalloidin (green), and BMSC-exos @ CeO_2 with PKH26 (red). Merged confocal fluorescent images display colocalization. Scale bar: 20 μm. (**b**) Effects of different treatments on cell proliferation: Hoechst 33,342-stained nuclei (blue) and EDU-stained nuclei (red) were shown, with merged images indicating colocalization. The white arrow points to the nucleus stained with EDU. Scale bar: 20 μm. The experiment was conducted independently three times with three samples per group. (**c**) Relative fluorescence intensity of EDU-labeled nuclei under different conditions. (**d**) CCK-8 assay measuring cytotoxicity of BMSC-exos @ CeO_2 and CeO_2 NPs in Hepa 1–6 cells; control cell viability was set at 100%. Conducted independently three times, three samples per group. (**e**) Effects of different treatments on intracellular ROS levels: cell nuclei stained with Hoechst 33,342 (blue) and superoxide signals with Dihydroethidium (DHE, red). Merged images show colocalization. Scale bar: 20 μm. Experiments independently conducted three times, three samples per group. (**f**) Relative fluorescence intensity of DHE-labeled ROS. (**g**) Activity of superoxide dismutase (SOD). (**h**) Catalase (CAT) activity. (**i**) Glutathione peroxidase (GPX) activity. (**j**) Superoxide anion scavenging ability. (**k**) Hydroxyl radical scavenging ability. Data was mean ± standard deviation of three biological replicates. Conducted independently three times, three samples per group. (**l**-**s**) Effects of different treatments on inflammatory factor levels: data was mean ± standard deviation of three biological replicates. Conducted independently three times, three samples per group. (**t**) Heat map of the relative distribution levels of anti-inflammatory/oxidative stress and antioxidant indices between groups: data was the mean of three biological replicates. Zero to One method used for data normalization. "*" indicates $P < 0.05$ compared to the DON group for BMSC-exos @ CeO_2, BMSC-exos, or CeO_2 NPs. Green to red represents low to high relative distribution levels of inflammatory cytokines or antioxidant indices

radicals, resulting in indirectly increasing activities of antioxidant enzymes such as GPX, SOD, and CAT, with optimal performance observed for the BMSC-exos @ CeO_2 (Fig. 2g-k). Additionally, BMSC-exos @ CeO_2 induced significant reductions in levels of inflammatory cytokines, including TNF-α, IL-17 A, IL-6, IL-2, IL-4 and IL-1β within DON treatment ($P<0.05$) (Fig. 2l-s). Finally, the heat-map further illustrated that the comprehensive anti-inflammatory, anti-oxidative stress and antioxidant activities associated with BMSC-exos @ CeO_2 were significantly better than those obtained from separate applications of either BMSC-exos or CeO_2 NPs alone (Fig. 2t).

Distribution and levels of BMSC-exos @ CeO_2 in mouse liver and pathological and liver function detection under the DON condition

To investigate the distribution and retention of BMSC-exos @ CeO_2 in mouse liver, we first observed in vivo fluorescence imaging. The results and figures demonstrated that DiR-labeled BMSC-exos @ CeO_2 could be detected in the mouse liver for 72 h following tail vein injection, while no background fluorescence was observed in the Control group (Fig. 3a). Ex vivo imaging further showed a similar phenomenon, and the fluorescence signals were localized and observed from the liver at 72 h post-injection. These data indicated that BMSC-exos @ CeO_2 could maintain 72 h in the liver (Fig. 3b-c). Meanwhile, results from the ICP-MS platform further revealed that the Ce concentration in CeO_2 NPs group was highest at 24 h, and there was no significance between 48 and 72 h ($P>0.05$). However, the Ce levels of the BMSC-exos @ CeO_2 group were higher than CeO_2 NPs group at 24 ($P<0.05$), 48 ($P<0.05$) and 72 h ($P<0.05$), respectively (Fig. 3d).

Besides, compared to the Control group, the serum ALT and AST levels in the DON group significantly increased ($P<0.05$). The BMSC-exos @ CeO_2 group significantly maintained lower levels of serum ALT levels ($P<0.05$) and AST levels ($P<0.05$) than DON group (Fig. 3e-f).

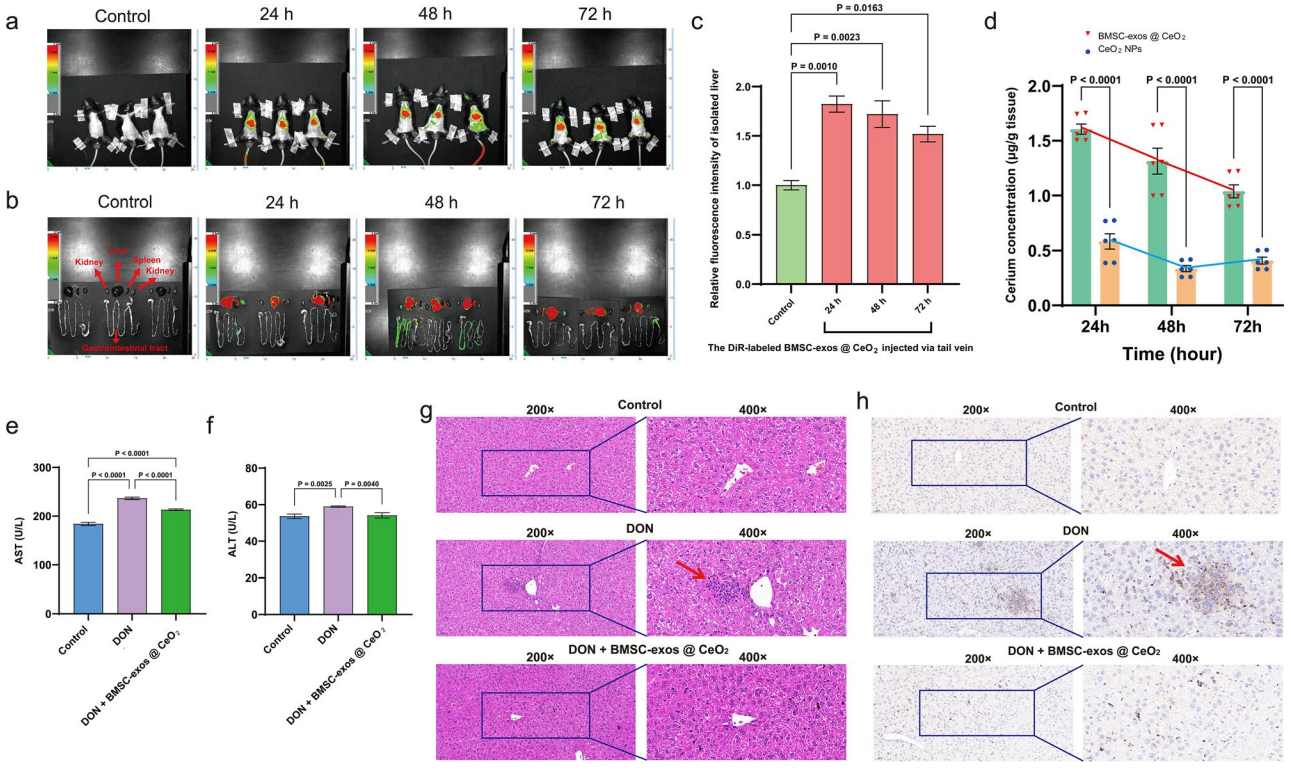

Fig. 3 Distribution of BMSC-exos @ CeO_2 in mouse liver and their protective effect against DON-induced liver injury. (**a**) In vivo distribution of BMSC-exos @ CeO_2: DiR-labeled BMSC-exos @ CeO_2 were injected via the tail vein, and their distribution was monitored at 24 h, 48 h, and 72 h using in vivo fluorescence imaging. Three biological samples per time point. (**b**) Organ distribution of BMSC-exos @ CeO_2: DiR-labeled BMSC-exos @ CeO_2 were injected via the tail vein, and organ distribution was assessed at the same time points using ex vivo fluorescence imaging. (**c**) Relative fluorescence intensity in the liver was shown, with green bars indicating background levels in the control group injected with PBS, and red bars showing the relative intensity post-injection compared to controls. Three biological samples per time point. (**d**) Ce levels in the liver measured by ICP-MS: Livers were collected at 24 h, 48 h, and 72 h post-injection of BMSC-exos @ CeO_2 and CeO_2, with Ce concentration evaluated using ICP-MS. Data represent mean ± standard deviation from three biological samples with two technical repeats. (**e**-**f**) Effects of BMSC-exos @ CeO_2 on serum ALT and AST levels: Data were shown as mean ± standard deviation. Six biological samples per group. (**g**) Hematoxylin and eosin (H&E) staining of mouse liver: Red arrows indicate lymphocyte infiltration. (**h**) Immunohistochemistry of mouse liver: Brown indicates Ly6g positive expression

Pathological examination also showed significant inflammatory cell infiltration around the central veins of liver lobules in the DON group, accompanied by hepatocyte deformation, swelling, and irregular arrangement. In contrast, the BMSC-exos @ CeO_2 group had a lower inflammatory response, indicating that this treatment could effectively alleviate DON-induced hepatic inflammation and other pathological damages (Fig. 3g). Meanwhile, as a GPI-anchored protein and a marker of neutrophils, Ly6g's positive expression indicated inflammatory processes. Immunohistochemistry (IHC) results further confirmed that positive expression of Ly6g significantly increased in the DON group compared to the control group. At the same time, BMSC-exos @ CeO_2 treatment significantly reduced Ly6g expression in the liver compared with DON group (Fig. 3h).

BMSC-exos @ CeO_2 alleviate DON-induced hepatic inflammatory response in mice associating with the JAK1/STAT3 signaling pathway

To explore the potential molecular mechanisms in this study, we employed 4D-DIA quantitative proteomics platform to uncover the interaction and signaling networks of differential proteins among groups. Qualitative and quantitative analyses of protein expression in mouse liver and quality control were conducted to assess the impact of BMSC-exos @ CeO_2 administration on liver protein expression patterns after DON exposure. Differentially expressed liver proteins among groups, GO analysis, and KEGG annotation results were provided in the supplementary materials (Sects. 1–6). Differential proteins were annotated using the KEGG database. KEGG enrichment analysis among groups was performed based on an enrichment ratio (DiffRatio/BgRatio) higher than 1, with $P<0.05$ as the standard. Significant KEGG enrichment results in different groups were shown in Fig. 4a-c.

Additionally, KEGG-enriched pathways in each group were presented using Venn diagrams to show the relationship of key differential metabolic pathways among groups. Differential metabolic pathways shared between the DON + BMSC-exos @ CeO_2 group and Control group, as well as between the DON and Control groups, were of primary concern, including the JAK-STAT signaling pathway and arachidonic acid metabolism (Fig. 4d). Our previous research demonstrated that BMSC-exos could mitigate DON-induced free radicals through their intrinsic PUFAs and significantly altered the profile of oxidative lipid metabolites associated with DON-induced liver damage, primarily enriched in the arachidonic acid metabolism pathway. Our current study leveraged the carrier potential of BMSC-exos to develop a composite formulation rich in PUFAs and CeO_2 NPs, which were designed as DON + BMSC-exos @ CeO_2. This composite synergistically reduces lipid peroxidation damage to hepatocyte membranes and other cellular components. Furthermore, various inflammatory mediators, such as IL-6, could activate the JAK1/STAT3 signaling pathway, thereby regulating the transcriptional activity of inflammatory genes and promoting the inflammatory response [62, 63].

To further testify results from the above mentioned, compared to the Control group, the expression levels of p-JAK1/JAK1 and p-STAT3/STAT3 were significantly increased in the DON group ($P<0.05$). Moreover, in DON + BMSC-exos @ CeO_2 group, the expression levels of p-JAK1/JAK1 and p-STAT3/STAT3 were significantly reduced compared to the DON group ($P<0.05$), with p-STAT3/STAT3 levels reduced by approximately 1-fold (Fig. 4e-f). Next, because the inflammatory cytokine could impact the JAK/STAT signaling pathway, we further measured inflammatory cytokine levels in mouse liver tissues and serum. Compared to the Control group, TNF-α, IL-17 A, IL-2, IL-4, and IL-6 levels were significantly increased in the DON group ($P<0.05$). In contrast, BMSC-exos @ CeO_2 group showed significantly lower levels of IL-2, IL-4, and IL-6 than the DON group ($P<0.05$) (Fig. 4g-l). In the serum, compared with the control group, IL-4 and IL-6 levels were significantly increased in the DON group ($P<0.05$). However, BMSC-exos @ CeO_2 group illustrated significantly lower IL-6 levels than the DON group ($P<0.05$) (Fig. 4m-r). These results suggested that BMSC-exos @ CeO_2 could inhibit inflammatory cytokine levels and inflammatory lesions.

Untargeted/targeted metabolomics reveal Oxylipins profiles in different groups

Observations of protein expression levels and protein interactions alone might have been dimensionally limited. Therefore, this study also employed LC-MS/MS platform-based untargeted/targeted metabolomics analysis on mouse liver. This method enabled an unbiased analysis of nearly all metabolite categories in samples, providing a multidimensional view of the logical and interactive relationship among DON treatment, protein molecules, metabolic pathways, and damage phenotypes.

Qualitative and quantitative analyses of metabolites and functional KEGG annotations among groups were provided in the supplementary materials (Sects. 7–11). Based on the results of differential metabolites, KEGG pathway enrichment analysis was conducted, revealing significant enrichment of linoleic acid, glycerophospholipid, arachidonic acid, and alpha-linolenic acid metabolism among groups (Fig. 5a, d and g). A comprehensive joint analysis of enrichment pathways for differentially expressed hepatic metabolites and proteins was performed. Bar graphs illustrating co-annotated KEGG pathways demonstrated a differential distribution and abundance of these metabolites and proteins within specific pathways

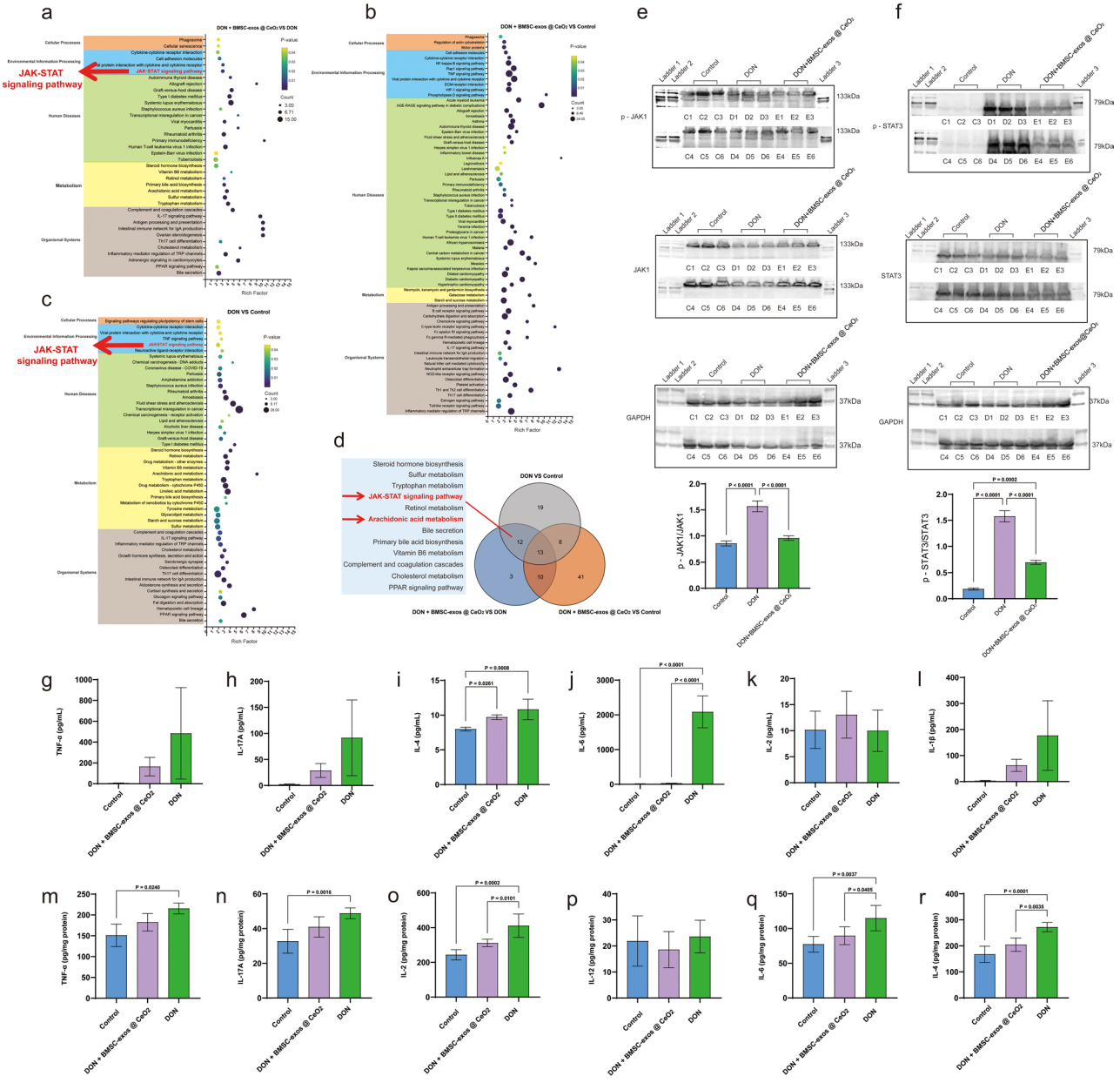

Fig. 4 Impact of BMSC-exos @ CeO_2 on liver protein functional pathways after DON exposure and their validation. (**a**-**c**) KEGG enrichment analysis of differentially expressed proteins: The x-axis represents the enrichment factor, and the y-axis shows KEGG pathways. Dot color and size indicate P-values and the number of differentially expressed proteins, respectively. (**d**) Venn diagram illustrating inter-group relationships of KEGG differential metabolic pathways: Analysis of KEGG pathways with a ratio of DiffRatio/BgRatio greater than 1 and P-value less than 0.05. Each circle represents a comparison group, overlapping sections show shared differential metabolic pathways, and non-overlapping sections indicate unique pathways. (**e**-**f**) Effects of BMSC-exos @ CeO_2 on p-JAK1/JAK1 and p-STAT3/STAT3 protein expression in DON-exposed mouse liver: Western blot lanes C1-C6 were controls, D1-D6 were the DON group, and E1-E6 were the DON + BMSC-exos @ CeO_2 group. Data were presented as mean ± standard deviation. (**g**-**l**) Effects of BMSC-exos @ CeO_2 on serum inflammatory factor levels in mice: Data shown as mean ± standard deviation. Six biological samples per group. (**m**-**r**) Effects of BMSC-exos @ CeO_2 on liver inflammatory factor levels in mice: Data shown as mean ± standard deviation. Six biological samples per group

(Fig. 5b, e and h). Notably, linoleic acid and arachidonic acid metabolism pathways consistently ranked among the top three across all comparative groups, highlighting a significant presence of these metabolites and proteins within these pathways. Additionally, bar graphs of KEGG co-enriched pathways presented pathways' enrichment P-values, with the top 50 pathways displayed based on proteomics data. Compared with the DON group vs. the control group and DON + BMSC-exos @ CeO_2 vs. DON groups, linoleic acid and arachidonic acid metabolic pathways were significantly enriched (Fig. 5c, f and i). The core target proteins with differentially expressed levels

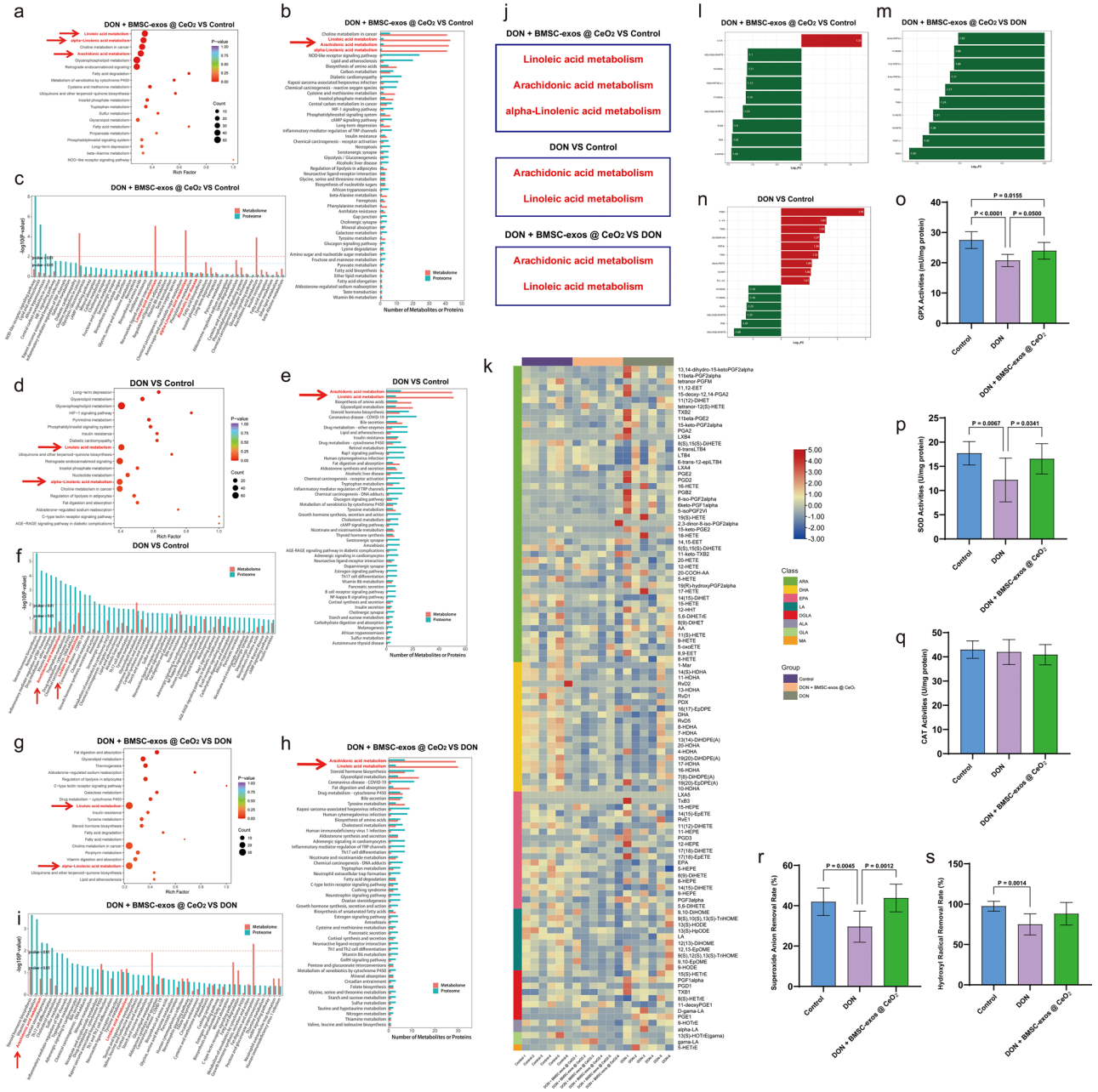

Fig. 5 Integrated analysis of differential metabolites and protein enrichment pathways in the liver. (**a**) Enrichment analysis of differential metabolites between groups: The y-axis represents pathway names, sorted by P-value; dot color and size indicate enrichment significance and the number of differential metabolites. The x-axis shows the pathway's Rich Factor. (**b**) Bar plot of KEGG pathways jointly annotated by differential analyses from two omics: The x-axis represents the number of differentially expressed proteins (green) and metabolites (red) annotated to each pathway, while the y-axis represents KEGG pathways. (**c**) Bar chart of KEGG pathways co-enriched by both omics analyses: The chart displays the P-values for pathway enrichment, showing the top 50 pathways based on protein analysis P-values. The x-axis shows KEGG pathway names; the y-axis displays enrichment P-values, with red and green indicating metabolomics and proteomics, respectively. (**d**-**f**) Joint KEGG pathway analysis of differential metabolites and proteins between DON and Control groups. (**g**-**i**) Joint KEGG pathway analysis of differential metabolites and proteins between DON + BMSC-exos @ CeO_2 and DON groups. (**j**) Key KEGG pathways identified in the integrated analysis of intergroup differential metabolites and proteins. (**k**) Overall sample clustering heat map: Samples were on the x-axis, metabolites on the y-axis. Colors represent normalized abundance values (red for high, blue for low). Group indicates sample grouping, and Class indicates substance classification. (**l**-**n**) Fold-change bar plot: The x-axis shows log_2 FC of differential metabolites, while the y-axis lists metabolites. Red bars indicate upregulated metabolites; green bars indicate downregulated metabolites. (**o**) GPx activity. (**p**) SOD activity. (**q**) CAT activity. (**r**) Superoxide anion scavenging capacity. (**s**) Hydroxyl radical scavenging capacity. Data were presented as mean ± standard deviation. Six biological samples per group

shared between the DON + BMSC-exos @ CeO_2 group and the DON group, as well as between the DON group and the Control group, were the focus of this study. Notably, Angptl3 (Angiopoietin-like 3), an essential regulator of lipid metabolism, played a critical role in regulating cholesterol, triglycerides, and glucose metabolism, and was involved in fatty acid synthesis and oxidation processes (Figures S11). Its expression levels were associated with various metabolic diseases, such as atherosclerosis and fatty liver disease. Studies have shown that regulating lipid metabolism by Angptl3 might affect the protective mechanisms of the liver through multiple signaling pathways. We further conducted a correlation analysis of the quantitative values of proteins and metabolites across all samples (Table S1). The results revealed that the Angptl3 protein was significantly correlated with several metabolites, including Ascorbic acid, Trigallic Acid, Equol 7-O-glucuronide, and Ergothioneine, which exhibited antioxidant and anti-inflammatory properties. Additionally, metabolites such as 2'-Deoxyuridine 5'-monophosphate and Febuxostat played crucial roles in energy and lipid metabolism (Table S2). These findings suggested that when using BMSC-exos @ CeO_2 to alleviate DON-induced liver injury, these metabolites and proteins had significant biological implications for antioxidation, anti-inflammation, and regulating energy metabolism homeostasis.

Additionally, hepatic oxidative lipidomics analysis data in different groups revealed the distribution heat map of oxylipins. We found that BMSC-exos @ CeO_2 or DON affected the pattern of oxylipins distribution/pattern, with metabolites derived from arachidonic acid precursors being the largest subset (Fig. 5k). Administration of BMSC-exos @ CeO_2 significantly reduced all differential oxidative lipid levels compared to the DON group (Fig. 5l-n). The reduction in specific pro-inflammatory oxidized lipids, such as 11-HEDE, 18-HETE, 11β-PGF2α, 8-iso-PGF2α, PGE1, 6-keto-PGF1α, and PGF1α, might inhibit oxidative stress, thereby reducing the synthesis of inflammatory mediators. This regulation could alleviate inflammation and tissue damage and was closely associated with inhibiting the JAK1/STAT3 pathway. The differential oxylipins among groups were presented in Table S3, and the KEGG Differential Abundance Score were also presented in Table S5.

We further assessed the antioxidant capacity in different groups. Compared to the Control group, DON group showed a significant reduction of SOD and GPX enzyme activities in livers ($P < 0.05$), whereas BMSC-exos @ CeO_2 treatment significantly enhanced these enzyme activities ($P < 0.05$). Moreover, DON exposure significantly impaired the superoxide anion and hydroxyl radical scavenging abilities in livers ($P < 0.05$). However, BMSC-exos @ CeO_2 treatment significantly enhanced superoxide anion scavenging ability ($P < 0.05$), while improving hydroxyl radical scavenging ability without significance ($P > 0.05$) (Fig. 5o-s). Thus, according to the above results, we suggested that the BMSC-exos @ CeO_2 could synergistically reduce DON-induced lipid peroxidation and maintain a rich content of unsaturated fatty acids for reducing damage on hepatocyte membranes or other cellular components and enhancing the defense abilities of antioxidants.

Untargeted/targeted metabolomics reveal energy metabolism in different groups

Metabolic and proteomic differences among groups were path-searched and regulatory interaction networks were analyzed through the KEGG database (Fig. 6a-c). Subsequently, a picture of the Venn diagram illustrated the relationship of key differential metabolite pathways and modules among groups, focusing on specific differential metabolic pathways and modules between DON + BMSC-exos @ CeO_2 and the DON group, where the AMPK was associated with the inflammatory response by restoring cellular energy homeostasis (Fig. 6d). Numerous studies suggested AMPK activation might have been a new strategic option for treating inflammatory diseases [64, 65], highlighting its association with unsaturated fatty acid metabolism and inflammatory regulation. Further targeted metabolomics analyses of energy metabolism products in mouse livers from different groups showed that both BMSC-exos @ CeO_2 and DON significantly altered the energy metabolite distribution pattern in mouse livers (Fig. 6e). The differential energy metabolites in different groups were presented in Table S4, and the KEGG Differential Abundance Score were presented in Table S5.

Finally, because DON influenced AMPK expression, thereby altering energy metabolism and cell homeostasis, Western blotting was further used to detect AMPK protein expression levels in different groups for testifying above. Compared to the Control group, p-AMPK/AMPK expression was significantly enhanced in DON group ($P < 0.05$). Meantime, DON + BMSC-exos @ CeO_2 group displayed a higher protein expression level of p-AMPK/AMPK compared to the Control group ($P < 0.05$) and protein expression levels about 1.2-fold higher than the DON group ($P < 0.05$, Fig. 6f). In summary, the alleviating effects of BMSC-exos @ CeO_2 on DON-induced oxidative stress and inflammatory response were closely related to the involvement of the AMPK and JAK1/STAT3 pathways.

Discussion

In this study, we investigated the toxic mechanisms of DON on the liver and presented a novel strategy for reducing its toxic effects. DON was a pervasive toxin that had multiple toxic effects on humans and animals,

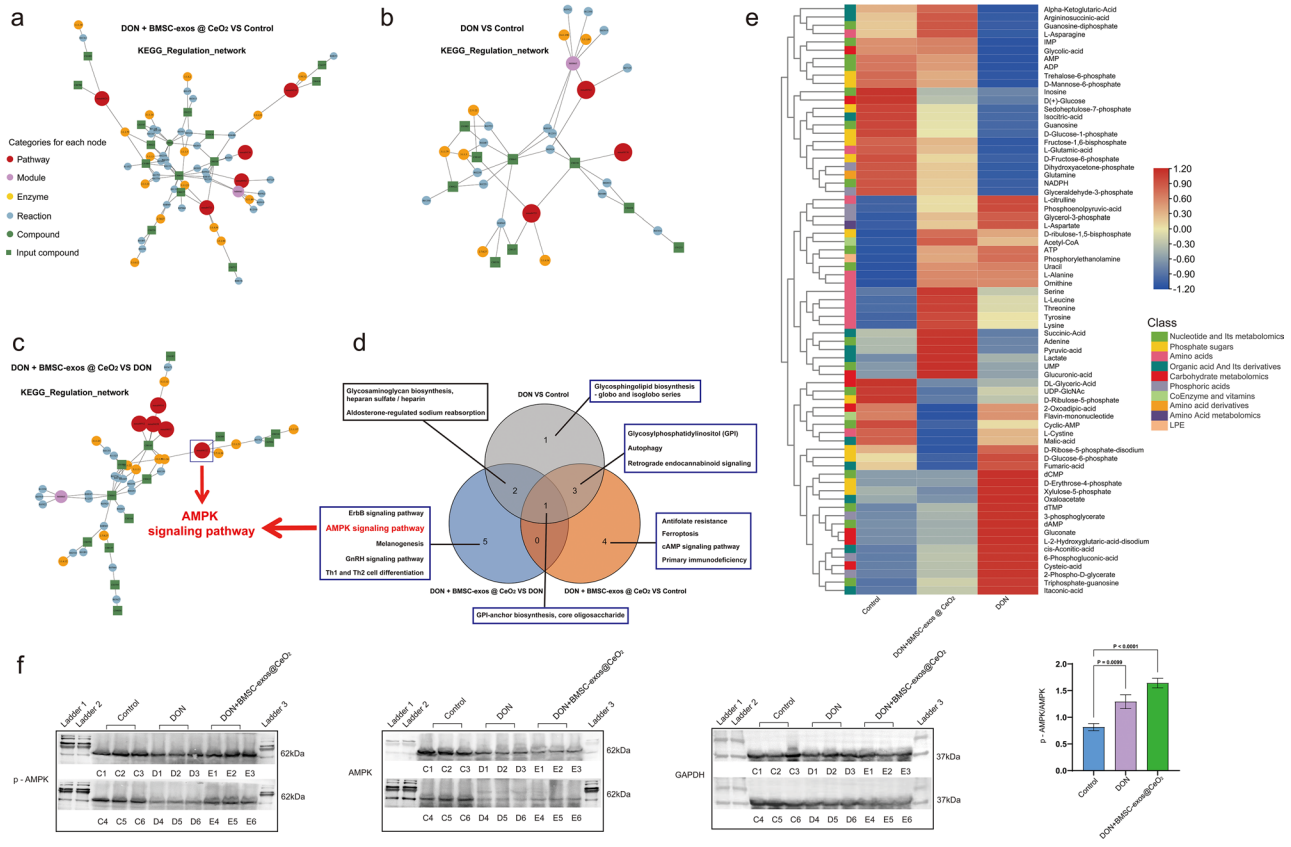

Fig. 6 Differential energy metabolism and effects on AMPK expression. (**a**-**c**) Regulatory network analysis of differential metabolites between groups. Red circles indicate differential metabolic pathways, yellow circles represent regulatory enzymes, green circles denote background substances, purple circles indicate molecular modules, blue circles represent chemical interactions, and green squares indicate differential metabolites. (**d**) Venn diagram showing the relationships between key differential metabolic pathways and modules among groups. Circles represent comparison groups; overlapping areas indicate shared differential pathways and modules, while non-overlapping areas denote unique ones. (**e**) Heat map of overall sample cluster averages: Samples were on the horizontal axis, metabolites on the vertical axis. Different colors represent normalized average values across groups, with red indicating high abundance and blue indicating low abundance. (**f**) Effects of BMSC-exos @ CeO_2 on AMPK and p-AMPK protein expression in the livers of DON-exposed mice: Western blot lanes C1-C6 were for the control group, D1-D6 were for the DON group, and E1-E6 were for the DON + BMSC-exos @ CeO_2 group. Data were presented as mean ± standard deviation

including acute and chronic symptoms [1–3]. Furthermore, DON was primarily metabolized and detoxified in the liver, where its induction of oxidative stress represented a key pathway leading to liver damage. Previous studies showed that DON exposure reduced liver antioxidant enzyme activity and elevated oxidative stress levels [66].

Recent research has highlighted the potential of CeO_2 NPs as antioxidants. The CeO_2 NPs transitioned between Ce^{3+} and Ce^{4+} states, where Ce^{3+} bound to reactive oxygen or nitrogen species and reduced them to peroxides and nitrates, while oxidizing itself to the Ce^{4+} state, similar to the function of SOD [28, 67]. This oxidation process was followed by the reduction of Ce^{4+} back to Ce^{3+}, which oxidized hydrogen peroxide into molecular oxygen, thereby mimicking catalase activity [67]. The radical scavenging capacity of CeO_2 NPs was renewable, functioning through a continuous $Ce^{3+} \rightarrow Ce^{4+} \rightarrow Ce^{3+}$ reaction cycle on their surface, offering an advantage over other antioxidants [68, 69]. These CeO_2 NPs were relatively inert under healthy physiological conditions, slowly dissolving into low-toxicity Ce^{3+} in the body and eventually being excreted through the urinary or fecal (hepatobiliary circulation) pathways [51, 68, 70]. This excellent biocompatibility and stability made CeO_2 NPs a promising candidate for antioxidant therapy.

Compared to traditional antioxidants such as SOD and vitamin C, the CeO_2 NPs offered the added benefit of reusability, as their capacity to scavenge reactive oxygen species remained sustained over time [71, 72]. Our study results also showed CeO_2 NPs significantly inhibited the oxidative stress and inflammatory response that DON induced in Hepa1-6 cells. Notably, CeO_2 NPs became active only in the presence of excess free radicals, thus minimizing the potential adverse effects associated with excessive free radical scavenging [72]. We further investigated the encapsulation of CeO_2 NPs within BMSC- exos as an innovative approach to mitigate the toxic effects of

DON on the liver. The combination of CeO_2 NPs with BMSC-exos offered several advantages. Previous studies demonstrated that the dispersion of CeO_2 NPs was critical for their efficacy. Reducing aggregation minimized immune system recognition and ensured a larger surface area-to-volume ratio, thereby enhancing their free radical scavenging capacity. Additionally, the particle size, solubility, and stability of CeO_2 NPs significantly influenced their cellular uptake and fate in vivo [73–75]. Therefore, previous studies often involved re-ultrasonication before administration to ensure uniform distribution; however, this method could not guarantee sustained dispersion in vivo. As excellent drug delivery carriers, exosomes were derived from cells and exhibited high biocompatibility. Their vesicular structure protected internal cargo from degradation and phagocytosis by immune cells. Moreover, exosomes possessed good permeability, and their nanoscale size and membrane structure enabled efficient intracellular delivery [76, 77]. Thus, loading CeO_2 NPs into BMSC-exos prevented aggregation, enhanced biocompatibility and permeability, and ensured safer and more effective functionality. This approach also provided an initial "defense line" against DON-induced oxidative damage. The rich PUFAs in exosomes contributed to synergistic antioxidant and anti-inflammatory effects [22]. Further exploration of CAT activity in the DON + BMSC-exos @ CeO_2 group revealed interesting results. Our previous studies showed that BMSC-exos intervention significantly increased SOD activity in mouse livers, with a strong positive correlation between Cu/Zn SOD and oxygen species targeted by BMSC-exos [22]. This indicated that BMSC-exos inherently enhanced SOD activity. When loaded with CeO_2 NPs, this effect might have been synergistically amplified. Additionally, DON exposure triggered cellular self-protection mechanisms, leading to higher antioxidant enzyme activity in the short term compared to the control group. Consequently, the DON + BMSC-exos @ CeO_2 group exhibited significantly higher CAT activity than the control group, though no significant difference was observed compared to the DON-only group. These differences may be attributed to the synergistic effects of BMSC-exos and CeO_2 NPs and the stress response induced by DON. Both in vitro and in vivo experiments confirmed the effectiveness of the BMSC-exos @ CeO_2 combination in alleviating DON-induced cell and liver damage. Therefore, this dual-functional delivery system, characterized by its antioxidant and protective properties, as well as biocompatibility, offered significant advantages over traditional methods. Compared to other nanocarrier systems, such as liposomes and polymer nanoparticles, which provided enhanced solubility and sustained release, exosome-based systems excelled in inherent biocompatibility and targeting efficiency. Our BMSC-exos @ CeO_2 system stood out due to its intrinsic biocompatibility and sustained scavenging activity, features uncommon in other nanoparticles. However, potential disadvantages included the complexity of exosome isolation and purification processes and the extensive characterization required to ensure consistency and safety in therapeutic applications.

Using a multi-level analysis that integrated proteomics and metabolomics, this study investigated the toxic effects and mechanisms of DON and the protective effects of BMSC-exos @ CeO_2. The 4D-DIA quantitative proteomics combined with LC-MS/MS untargeted and targeted metabolomics analyses identified expression patterns of numerous differential proteins and metabolites, along with the biological pathways they influenced. This analysis highlighted the involvement of the JAK-STAT signaling pathway and arachidonic acid metabolism in DON-induced liver injury. Furthermore, our results demonstrated that the intervention of BMSC-exos @ CeO_2 significantly impacted the regulation of these pathways, highlighting its protective potential. KEGG database annotation and enrichment analysis further elucidated key signaling networks, particularly those involved in inflammatory and metabolic pathways. The most differentially expressed metabolites and proteins were found in the linoleic acid and arachidonic acid metabolism pathways. On the one hand, this finding corroborated our hypothesis that DON-induced lipid peroxidation primarily affected the biomembrane, serving as the "main battlefield" or "first line of beneficial defense". BMSC-exos @ CeO_2, rich in unsaturated fatty acids and CeO_2 NPs, synergistically mitigated DON-induced lipid peroxidation damage to liver cell membranes and other cellular components. The affected metabolic pathways, including unsaturated fatty acid metabolism and associated damage phenotypes, formed a complex multi-factor regulatory network. On the other hand, studies showed that AMPK, an energy-sensing enzyme, played a central role in maintaining cellular energy balance and interacted intricately with PUFAs metabolism. Metabolites of PUFAs, such as epoxyeicosatrienoic acids (EETs) derived from arachidonic acid, activated AMPK and promoted autophagy, which helped inhibit TNF-α-induced endothelial cell apoptosis [78]. Additionally, AMPK regulated PUFAs metabolism, such as conjugated linoleic acid (CLA), by influencing key enzymes in fatty acid synthesis and oxidation, including acetyl-CoA carboxylase (ACC) and sterol regulatory element-binding protein 1c (SREBP1c), thereby modulating lipid metabolism and reducing inflammatory responses [79]. Linoleic acid also activated AMPK via the SQSTM1 (P62) and Kelch-like ECH-associated protein 1 (Keap1) complex, connecting the autophagy and antioxidant systems to enhance cellular antioxidant capacity and reduce oxidative stress [80]. These interactions revealed that under

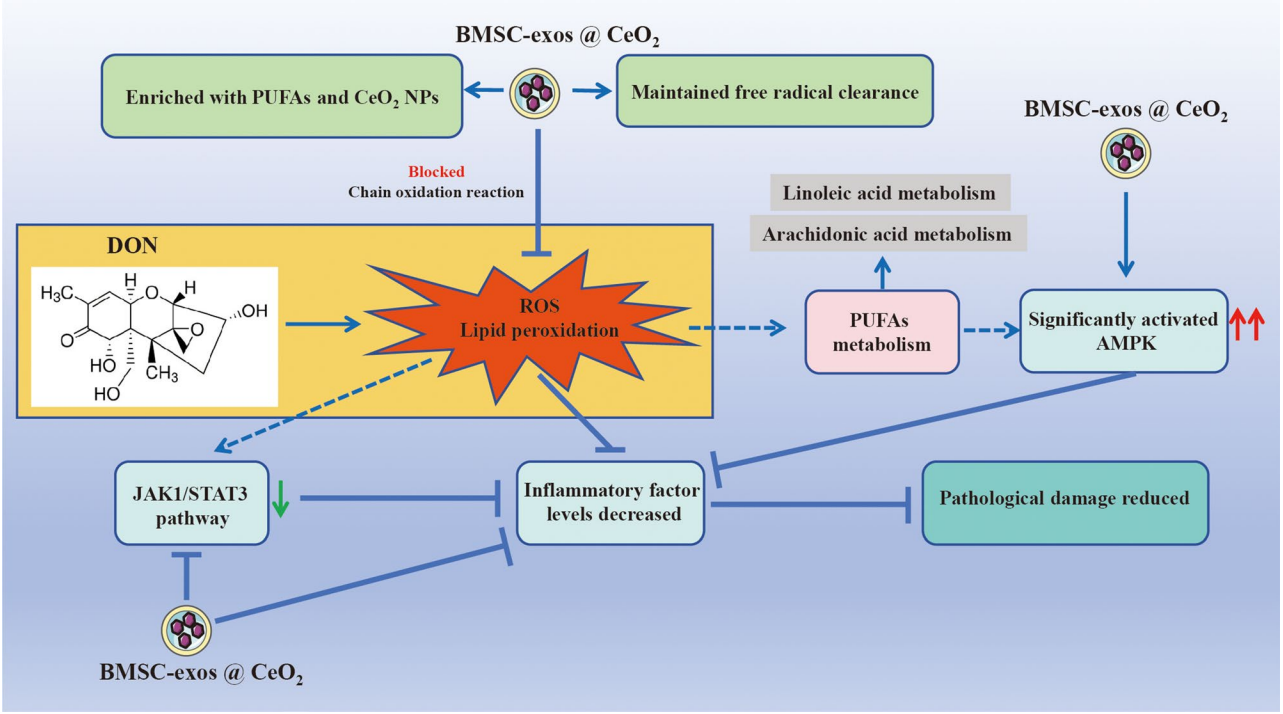

Fig. 7 Schematic diagrams of research results. Schematic diagram illustrating the synergistic protective effects from BMSC-exos @ CeO_2 administration under the DON condition

the regulation of BMSC-exos @ CeO_2, AMPK and PUFAs metabolism played a synergistic role in antioxidation and anti-inflammation.

Proteomic analysis revealed that the JAK-STAT signaling pathway significantly alleviated DON-induced liver injury by BMSC-exos @ CeO_2. The metabolomic analysis further indicated that the AMPK signaling pathway was a unique differential metabolic pathway between the DON + BMSC-exos @ CeO_2 group and the DON group. AMPK inhibited inflammatory responses by restoring cellular energy homeostasis, and numerous studies suggested that activating AMPK might represent a potential new strategy for treating inflammatory diseases [64, 81]. Our research demonstrated that BMSC-exos @ CeO_2 administration significantly reduced the levels of IL-2, IL-4, and IL-6 in the livers of DON-exposed mice ($P < 0.05$) and also significantly decreased serum IL-6 levels in DON-exposed mice ($P < 0.05$). Based on these findings, it was inferred that DON induced an increase in PUFAs metabolism through oxidative stress, while liver cells initiated self-rescue mechanisms by upregulating AMPK expression. BMSC-exos @ CeO_2 could block the peroxidation chain reaction, further activated AMPK expression, alleviated oxidative stress, and inhibited JAK1/STAT3 pathway activation, suppressing inflammatory response occurrence or exacerbation (Fig. 7). Therefore, it was concluded that the alleviation of DON-induced inflammatory responses by BMSC-exos @ CeO_2 was closely related to the interaction and modulation of the AMPK/JAK1/STAT3 pathways, providing new evidence for mitigating DON-induced inflammatory damage.

Oxidative lipidomics analysis indicated that BMSC-exos @ CeO_2 could reduce DON-induced abnormal lipid metabolism and improved antioxidant capacity, which was related to enhanced superoxide anion scavenging ability and increased antioxidant enzyme activity. Energy metabolism analysis further revealed the activation of the AMPK signaling pathway's important role in the protective effect mediated by BMSC-exos @ CeO_2, highlighting the close connection between fatty acid metabolism and oxidative stress and inflammatory response regulation. Additionally, it was worth exploring the observation that, although SOD activity in the DON + BMSC-exos @ CeO_2 group was significantly increased compared to both the control and DON-only groups, the comprehensive analysis of differential metabolites and protein enrichment pathways in the liver did not reveal significant enrichment of antioxidant enzyme-related pathways. To address this inconsistency, we considered the unique antioxidant mechanism of CeO_2 NPs. Previous studies showed that CeO_2 NPs directly mimicked the effects of antioxidant enzymes by cycling between Ce^{3+} and Ce^{4+} oxidation states [28, 29, 82, 83], rather than by stimulating the expression of intracellular antioxidant enzymes. Consequently, this direct antioxidant

mechanism might have explained the lack of significant enrichment of antioxidant enzyme-related pathways in the metabolic pathway enrichment analysis. These findings provided a detailed understanding of the molecular mechanisms involved, supporting further exploration of DON toxicity and possible interventions. This study provided a comprehensive understanding of the molecular mechanisms involved, supporting further exploration of vomitoxin toxicity and potential intervention strategies. A limitation of this study was that it focused solely on the protective effects of BMSC-exos @ CeO_2 against DON-induced liver damage. Future research should investigate the systemic impact of BMSC-exos @ CeO_2 on other organs affected by DON toxicity. Additionally, while animal models offered valuable insights, caution was needed when extrapolating these findings to human health. In the future, the BMSC-exos @ CeO_2 system held promise for developing therapies targeting liver diseases exacerbated by oxidative stress, but ensuring safety and efficacy remained critical for clinical translation. This system could also be applied to protect livestock consuming DON-contaminated feed, thereby reducing economic losses in the livestock industry and enhancing food safety. To ensure economic feasibility, challenges related to scaling up production and improving cost-effectiveness must have been addressed.

Conclusion

This study investigated the potential mechanisms and effects of BMSC-exos @ CeO_2 in mitigating hepatic injury induced by DON. The synthesized nanoparticles exhibited favorable bioavailability, characterized by optimal particle size and surface charge properties, which promoted Hepa 1–6 cell proliferation while reducing oxidative stress and inflammation. In vivo studies demonstrated their superior liver biodistribution and persistence, significantly decreasing inflammatory cytokine levels and modulation of the JAK1/STAT3 signaling pathway. Multi-dimensional metabolomics analysis further revealed that these nanoparticles protected against DON-induced liver injury by modulating energy metabolism and oxidative stress. Overall, BMSC-exos @ CeO_2 exhibited enhanced protective effects against liver damage through synergistic antioxidant and anti-inflammatory mechanisms, offering promising insights for the future treatment of DON-related liver diseases.

Supplementary Information

The online version contains supplementary material available at https://doi.org/10.1186/s12951-025-03316-y.

Supplementary Material 1

Supplementary Material 2

Acknowledgements

The authors sincerely appreciate the provision of experimental instruments from the Medical sub-center of the Analytical and Testing Center, Huazhong University of Science and Technology. We also thank Wuhan Metware Biotechnology Co., LTD., Wuhan, China, for the assistance in the metabolome analysis.

Author contributions

Z. M.: Writing – original draft, Formal analysis, Conceptualization. M. T.: Data curation. S. X.: Methodology. X. Z.: Formal analysis. Z. Z.: Methodology. L. Y.: Formal analysis. A. N.: Writing – review & editing. L. L.: Methodology. W. Y.: Project administration, Funding acquisition, Conceptualization, Writing – review & editing.

Funding

This work was supported by the National Key Research and Development Program of China (grant No 2022YFC3600600 from W.Y) and National Natural Science Foundation of China (grant No. 82173521 and 82473635 from W.Y).

Data availability

No datasets were generated or analysed during the current study.

Declarations

Ethics and consent to Participate

All animal housing and experimental processes adhered strictly to the "Regulations on the Administration of Laboratory Animals in China". Experiments involving mice and the protocols were approved by the Institutional Animal Care and Use Committee of Huazhong University of Science and Technology (IACUC Number: 3622).

Competing interests

The authors declare no competing interests.

Author details

[1]Department of Nutrition and Food Hygiene, Hubei Key Laboratory of Food Nutrition and Safety, Tongji Medical College, Huazhong University of Science and Technology, Hangkong Road 13, Wuhan 430030, China
[2]Department of Toxicology, School of Public Health, Guangxi Key Laboratory of Environment and Health Research, Guangxi Medical University, Nanning, Guangxi 530021, China
[3]Department of Nutrition and Food Hygiene and MOE Key Lab of Environment and Health, School of Public Health, Tongji Medical College, Huazhong University of Science and Technology, Hangkong 14 Road 13, Wuhan, Wuhan 430030, China
[4]NHC Specialty Laboratory of Food Safety Risk Assessment and Standard Development, Tongji Medical College, Huazhong University of Science and Technology, Hangkong Road 13, Wuhan 430030, China
[5]Department of Traumatology, BG Trauma Center, University of Tübingen, Schnarrenbergstr. 95, 72076 Tübingen, Germany

Received: 1 December 2024 / Accepted: 11 March 2025
Published online: 17 March 2025

References

1. Gab-Allah MA, Tahoun IF, Yamani RN, Rend EA, Shehata AB. Natural occurrence of Deoxynivalenol, Nivalenol and deoxynivalenol-3-glucoside in cereal-derived products from Egypt. Food Control. 2022;137.
2. Belasli A, Herrera M, Ariño A, Djenane D. Occurrence and exposure assessment of major Mycotoxins in foodstuffs from Algeria. Toxins. 2023;15.
3. Vin K, Rivière G, Leconte S, Cravedi JP, Fremy JM, Oswald IP, Roudot AC, Vasseur P, Jean J, Hulin M, Sirot V. Dietary exposure to Mycotoxins in the French infant total diet study. Food Chem Toxicol. 2020;140.
4. Hooft JM, Bureau DP. Deoxynivalenol: mechanisms of action and its effects on various terrestrial and aquatic species. Food Chem Toxicol. 2021;157.
5. Jin J, Beekmann K, Ringo E, Rietjens IMCM, Xing FG. Interaction between food-borne Mycotoxins and gut microbiota: A review. Food Control. 2021;126.

6. Tan T, Chen T, Zhu W, Gong L, Yan Y, Li Q, Chen L, Li Y, Liu J, Li Y, et al. Adverse associations between maternal Deoxynivalenol exposure and birth outcomes: a prospective cohort study in China. BMC Med. 2023;21:328.
7. Amuzie CJ, Pestka JJ. Suppression of insulin-like growth factor acid-labile subunit expression–a novel mechanism for deoxynivalenol-induced growth retardation. Toxicol Sci. 2010;113:412–21.
8. Voss KA. A new perspective on Deoxynivalenol and growth suppression. Toxicol Sci. 2010;113:281–3.
9. Tang M, Yuan DX, Liao P. Berberine improves intestinal barrier function and reduces inflammation, immunosuppression, and oxidative stress by regulating the NF-κB/MAPK signaling pathway in deoxynivalenol-challenged piglets. Environ Pollut. 2021;289.
10. Zhang X, Jiang L, Geng C, Cao J, Zhong L. The role of oxidative stress in deoxynivalenol-induced DNA damage in HepG2 cells. Toxicon. 2009;54:513–8.
11. Nagy CM, Fejer SN, Berek L, Molnar J, Viskolcz B. Hydrogen bondings in Deoxynivalenol (DON) conformations - A density functional study. J Mol Structure-Theochem. 2005;726:55–9.
12. Chen X, Ma J, Chen H. Induction of autophagy via the ROS-dependent AMPK/mTOR pathway protects Deoxynivalenol exposure grass carp hepatocytes damage. Fish Shellfish Immunol. 2023;135:108687.
13. Tang X, Zeng Y, Xiong K, Li M. The inflammatory injury of Porcine small intestinal epithelial cells induced by Deoxynivalenol is related to the decrease in glucose transport. J Anim Sci. 2024;102.
14. Wang X, Liu Q, Ihsan A, Huang L, Dai M, Hao H, Cheng G, Liu Z, Wang Y, Yuan Z. JAK/STAT pathway plays a critical role in the Proinflammatory gene expression and apoptosis of RAW264.7 cells induced by trichothecenes as DON and T-2 toxin. Toxicol Sci. 2012;127:412–24.
15. Gan F, Lin ZM, Tang JY, Chen XX, Huang KH. Deoxynivalenol at No-Observed Adverse-Effect levels aggravates DSS-Induced colitis through the JAK2/STAT3 signaling pathway in mice. J Agric Food Chem 2023;71:4144–52. https://doi.org/10.1021/acs.jafc.3c00252
16. Zhang Z, Fan K, Meng J, Nie D, Zhao Z, Han Z. Deoxynivalenol hijacks the pathway of Janus kinase 2/signal transducers and activators of transcription 3 (JAK2/STAT-3) to drive caspase-3-mediated apoptosis in intestinal Porcine epithelial cells. Sci Total Environ. 2023;864:161058.
17. Liao Y, Peng Z, Xu S, Meng Z, Li D, Zhou X, Zhang R, Shi S, Hao L, Liu L, Yang W. Deoxynivalenol exposure induced colon damage in mice independent of the gut microbiota. Mol Nutr Food Res. 2023;67:e2300317.
18. Yang LN, Xu S, Tang M, Zhou X, Liao Y, Nussler AK, Liu L, Yang W. The circadian rhythm gene Bmal1 ameliorates acute deoxynivalenol-induced liver damage. Arch Toxicol. 2023;97:787–804.
19. Zhang ZQ, Wang SB, Wang RG, Zhang W, Wang PL, Su XO. Phosphoproteome analysis reveals the molecular mechanisms underlying Deoxynivalenol-Induced intestinal toxicity in IPEC-J2 cells. Toxins (Basel). 2016;8.
20. Meng Z, Wang L, Liao Y, Peng Z, Li D, Zhou X, Liu S, Li Y, Nussler AK, Liu L et al. The protective effect of Heme Oxygenase-1 on liver injury caused by DON-Induced oxidative stress and cytotoxicity. Toxins (Basel). 2021;13.
21. Liao Y, Peng Z, Wang L, Li D, Yue J, Liu J, Liang C, Liu S, Yan H, Nussler AK, et al. Long noncoding RNA Gm20319, acting as competing endogenous RNA, regulated GNE expression by sponging miR-7240-5p to involve in deoxynivalenol-induced liver damage in vitro. Food Chem Toxicol. 2020;141:111435.
22. Meng Z, Liao Y, Peng Z, Zhou X, Zhou H, Nussler AK, Liu L, Yang W. Bone marrow mesenchymal Stem-Cell-Derived exosomes ameliorate Deoxynivalenol-Induced mice liver damage. Antioxid (Basel). 2023;12.
23. Psaraki A, Ntari L, Karakostas C, Korrou-Karava D, Roubelakis MG. Extracellular vesicles derived from mesenchymal stem/stromal cells: the regenerative impact in liver diseases. Hepatology. 2022;75:1590–603.
24. Jafarinia M, Alsahebfosoul F, Salehi H, Eskandari N, Ganjalikhani-Hakemi M. Mesenchymal stem Cell-Derived extracellular vesicles: A novel Cell-Free therapy. Immunol Investig. 2020;49:758–80.
25. Kalluri R, LeBleu VS. The biology, function, and biomedical applications of exosomes. Science. 2020;367.
26. Borst JW, Visser NV, Kouptsova O, Visser AJWG. Oxidation of unsaturated phospholipids in membrane bilayer mixtures is accompanied by membrane fluidity changes. Biochim Et Biophys Acta-Molecular Cell Biology Lipids. 2000;1487:61–73.
27. Dowding JM, Dosani T, Kumar A, Seal S, Self WT. Cerium oxide nanoparticles scavenge nitric oxide radical (NO). Chem Commun (Camb). 2012;48:4896–8.
28. Korsvik C, Patil S, Seal S, Self WT. Superoxide dismutase mimetic properties exhibited by vacancy engineered ceria nanoparticles. Chem Commun (Camb). 2007;10:1056–8. https://doi.org/10.1039/b615134e
29. Cafun JD, Kvashnina KO, Casals E, Puntes VF, Glatzel P. Absence of Ce3 + sites in chemically active colloidal ceria nanoparticles. ACS Nano. 2013;7:10726–32.
30. Amin KA, Hassan MS, Awad el ST, Hashem KS. The protective effects of cerium oxide nanoparticles against hepatic oxidative damage induced by monocrotaline. Int J Nanomed. 2011;6:143–9.
31. Tian Y, Zhang Y, Zhao J, Luan F, Wang Y, Lai F, Ouyang D, Tao Y. Combining MSC exosomes and cerium oxide nanocrystals for enhanced dry eye syndrome therapy. Pharmaceutics. 2023;15.
32. Wei P, Wang Y, Feng H, Zhang F, Ji Z, Zhang K, Zhang Q, Jiang L, Qian Y, Fu Y. Gene-Engineered Cerium-Exosomes mediate atherosclerosis therapy through remodeling of the inflammatory microenvironment and DNA damage repair. Small. 2024;20:e2404463. https://doi.org/10.1002/smll.202404463
33. Fernandez-Varo G, Perramon M, Carvajal S, Oro D, Casals E, Boix L, Oller L, Macias-Munoz L, Marfa S, Casals G, et al. Bespoken nanoceria: an effective treatment in experimental hepatocellular carcinoma. Hepatology. 2020;72:1267–82.
34. Ahmadi S, Dadashpour M, Abri A, Zarghami N. Long-term proliferation and delayed senescence of bone marrow-derived human mesenchymal stem cells on Metformin co-embedded HA/Gel electrospun composite nanofibers. J Drug Deliv Sci Technol. 2023;80.
35. Kamalipooya S, Fahimirad S, Abtahi H, Golmohammadi M, Satari M, Dadashpour M, Nasrabadi D. Diabetic wound healing function of PCL/cellulose acetate nanofiber engineered with Chitosan/cerium oxide nanoparticles. Int J Pharm. 2024;653:123880.
36. Yasamineh S, Kalajahi HG, Yasamineh P, Gholizadeh O, Youshanlouei HR, Matloub SK, Mozafari M, Jokar E, Yazdani Y, Dadashpour M. Spotlight on therapeutic efficiency of mesenchymal stem cells in viral infections with a focus on COVID-19. Stem Cell Res Ther. 2022;13.
37. Serati-Nouri H, Rasoulpoor S, Pourpirali R, Sadeghi-Soureh S, Esmaeilizadeh N, Dadashpour M, Roshangar L, Zarghami N. In vitro expansion of human adipose-derived stem cells with delayed senescence through dual stage release of Curcumin from mesoporous silica nanoparticles/electrospun nanofibers. Life Sci. 2021;285.
38. Mofarrah M, Jafari-Gharabaghlou D, Dadashpour M, Zarghami N. Fabricating ZSM-5 zeolite/ Polycaprolactone nano-fibers co-loaded with dexamethasone and ascorbic acid: potential application in osteogenic differentiation of human adipose-derived stem cells. J Drug Deliv Sci Technol. 2023;79.
39. Huseynov E, Khalilov R, Mohamed AJ. Novel nanomaterials for hepatobiliary diseases treatment and future perspectives. Adv Biology Earth Sci. 2024;9.
40. Khalilov R, Nasibova A, Kavetskyy T, Kazımlı L, Keskin C, Bayramova M. Interactions of nanoparticles and biological systems. Adv Biology Earth Sci. 2024;9.
41. Welsh JA, Goberdhan DCI, O'Driscoll L, Buzas EI, Blenkiron C, Bussolati B, Cai HJ, Di Vizio D, Driedonks TAP, Erdbrügger U et al. Minimal information for studies of extracellular vesicles (MISEV2023): from basic to advanced approaches. J Extracell Vesicles. 2024;13.
42. Gao F, Tang Y, Liu WL, Zou MZ, Huang C, Liu CJ, Zhang XZ. Intra/Extracellular lactic acid exhaustion for synergistic metabolic therapy and immunotherapy of tumors. Adv Mater. 2019;31:e1904639.
43. Adebayo OA, Akinloye O, Adaramoye OA. Cerium oxide nanoparticles attenuate oxidative stress and inflammation in the liver of Diethylnitrosamine-Treated mice. Biol Trace Elem Res. 2020;193:214–25.
44. Shen B, Zhu Y, Kim Y, Zhou X, Sun H, Lu Z, Lee M. Autonomous helical propagation of active toroids with mechanical action. Nat Commun. 2019;10:1080.
45. Ma X, Luo S, Hua Y, Seetharaman S, Zhu X, Hou J, Zhang L, Wang W, Sun Y. An alumina phase induced composite transition shuttle to stabilize carbon capture cycles. Nat Commun. 2024;15:7556.
46. Meng Z, Zhou D, Lv D, Gan Q, Liao Y, Peng Z, Zhou X, Xu S, Chi P, Wang Z, et al. Human milk extracellular vesicles enhance muscle growth and physical performance of immature mice associating with Akt/mTOR/p70s6k signaling pathway. J Nanobiotechnol. 2023;21:304.
47. Wu G, Zhang Z, Chen X, Yu Q, Ma X, Liu L. Chemosensitization effect of cerium oxide nanosheets by suppressing drug detoxification and efflux. Ecotoxicol Environ Saf. 2019;167:301–8.
48. Zhou L, Tang S, Li F, Wu Y, Li S, Cui L, Luo J, Yang L, Ren Z, Zhang J, et al. Ceria nanoparticles prophylactic used for renal ischemia-reperfusion injury treatment by attenuating oxidative stress and inflammatory response. Biomaterials. 2022;287:121686.
49. Zhen K, Wei X, Zhi Z, Shang S, Zhang S, Xu Y, Fu X, Cheng L, Yao J, Li Y et al. Circulating extracellular vesicles from heart failure patients inhibit human cardiomyocyte activities. J Cardiovasc Transl Res 2024;17:1–18. https://doi.org/10.1007/s12265-024-10571-1

50. Mao X, Li J, Xie X, Chen S, Huang Q, Mu P, Jiang J, Deng Y. Deoxynivalenol induces caspase-3/GSDME-dependent pyroptosis and inflammation in mouse liver and HepaRG cells. Arch Toxicol. 2022;96:3091–112.
51. Oró D, Yudina T, Fernández-Varo G, Casals E, Reichenbach V, Casals G, de la Presa BG, Sandalinas S, Carvajal S, Puntes V, Jiménez W. Cerium oxide nanoparticles reduce steatosis, portal hypertension and display anti-inflammatory properties in rats with liver fibrosis. J Hepatol. 2016;64:691–8.
52. Meier F, Brunner AD, Koch S, Koch H, Lubeck M, Krause M, Goedecke N, Decker J, Kosinski T, Park MA, et al. Online parallel Accumulation-Serial fragmentation (PASEF) with a novel trapped ion mobility mass spectrometer. Mol Cell Proteom. 2018;17:2534–45.
53. Ross PL, Huang YN, Marchese JN, Williamson B, Parker K, Hattan S, Khainovski N, Pillai S, Dey S, Daniels S, et al. Multiplexed protein quantitation in Saccharomyces cerevisiae using amine-reactive isobaric tagging reagents. Mol Cell Proteom. 2004;3:1154–69.
54. Wu J, Xie X, Liu Y, He J, Benitez R, Buckanovich RJ, Lubman DM. Identification and confirmation of differentially expressed fucosylated glycoproteins in the serum of ovarian cancer patients using a lectin array and LC-MS/MS. J Proteome Res. 2012;11:4541–52.
55. Yu F, Haynes SE, Teo GC, Avtonomov DM, Polasky DA, Nesvizhskii AI. Fast quantitative analysis of TimsTOF PASEF data with MSFragger and ionquant. Mol Cell Proteom. 2020;19:1575–85.
56. Liang L, Rasmussen MLH, Piening B, Shen XT, Chen SJ, Röst H, Snyder JK, Tibshirani R, Skotte L, Lee NC, et al. Metabolic dynamics and prediction of gestational age and time to delivery in pregnant women. Cell. 2020;181:1680–.
57. Kaddurah-Daouk R, Kristal BS, Weinshilboum RM. Metabolomics: A global biochemical approach to drug response and disease. Annu Rev Pharmacol Toxicol. 2008;48:653–83.
58. Lu D, Lin ZY, Wang R, Chen Z, Zhuo JY, Xu L, Pan LH, Li HH, Yang XY, He CY et al. Multi-omics profiling reveals Chitinase-3-like protein 1 as a key mediator in the crosstalk between sarcopenia and liver cancer. Redox Biol. 2022;58.
59. Zhang N, Ji Q, Chen Y, Wen X, Shan F. TREM2 deficiency impairs the energy metabolism of Schwann cells and exacerbates peripheral neurological deficits. Cell Death Dis. 2024;15:193.
60. Peng Z, Liao YX, Wang XQ, Chen LK, Wang LL, Qin CY, Wang ZT, Cai MY, Hu JW, Li D, et al. Heme oxygenase-1 regulates autophagy through carbon-oxygen to alleviate deoxynivalenol-induced hepatic damage. Arch Toxicol. 2020;94:573–88.
61. Li B, Zhang Q, Du W, Wu J, Cheng J, Zhang Y, Gao R, Zhao X, Jiang L, Wu Y, et al. Reshaping cardiac microenvironments by macrophage-derived extracellular vesicles-coated Pd@CeO_2 heterostructures for myocardial ischemia/reperfusion injury therapy. Mater Today. 2023;65:47–61.
62. Xue C, Yao QF, Gu XY, Shi QM, Yuan X, Chu QF, Bao ZY, Lu J, Li LJ. Evolving cognition of the JAK-STAT signaling pathway: autoimmune disorders and cancer. Signal Transduct Target Therapy. 2023;8.
63. Murakami M, Hibi M, Nakagawa N, Nakagawa T, Yasukawa K, Yamanishi K, Taga T, Kishimoto T. IL-6-induced homodimerization of gp130 and associated activation of a tyrosine kinase. Science. 1993;260:1808–10.
64. Yuan YY, Wang F, Liu XX, Shuai B, Fan H. The role of AMPK signaling in ulcerative colitis. Drug Des Dev Therapy. 2023;17:3855–75.
65. Tong X, Ganta RR, Liu Z. AMP-activated protein kinase (AMPK) regulates autophagy, inflammation and immunity and contributes to osteoclast differentiation and functionabs. Biol Cell. 2020;112:251–64.
66. Hou YJ, Zhao YY, Xiong B, Cui XS, Kim NH, Xu YX, Sun SC. Mycotoxin-containing diet causes oxidative stress in the mouse. PLoS ONE. 2013;8:e60374.
67. Baldim V, Bedioui F, Mignet N, Margaill I, Berret JF. The enzyme-like catalytic activity of cerium oxide nanoparticles and its dependency on Ce(3+) surface area concentration. Nanoscale. 2018;10:6971–80.
68. Colon J, Herrera L, Smith J, Patil S, Komanski C, Kupelian P, Seal S, Jenkins DW, Baker CH. Protection from radiation-induced pneumonitis using cerium oxide nanoparticles. Nanomed. 2009;5:225–31.
69. Das M, Patil S, Bhargava N, Kang JF, Riedel LM, Seal S, Hickman JJ. Autocatalytic ceria nanoparticles offer neuroprotection to adult rat spinal cord neurons. Biomaterials. 2007;28:1918–25.
70. Chen Q, Chen JW, Yang ZJ, Xu J, Xu LG, Liang C, Han X, Liu Z. Nanoparticle-Enhanced radiotherapy to trigger robust cancer immunotherapy. Adv Mater. 2019;31.
71. Li M, Shi P, Xu C, Ren JS, Qu XG. Cerium oxide caged metal chelator: anti-aggregation and anti-oxidation integrated HO-responsive controlled drug release for potential Alzheimer's disease treatment. Chem Sci. 2013;4:2536–42.
72. Xu C, Lin YH, Wang JS, Wu L, Wei WL, Ren JS, Qu XG. Nanoceria-Triggered synergetic drug release based on ceo-Capped mesoporous silica Host-Guest interactions and switchable enzymatic activity and cellular effects of ceo. Adv Healthc Mater. 2013;2:1591–9.
73. Oro D, Yudina T, Fernandez-Varo G, Casals E, Reichenbach V, Casals G, Gonzalez de la Presa B, Sandalinas S, Carvajal S, Puntes V, Jimenez W. Cerium oxide nanoparticles reduce steatosis, portal hypertension and display anti-inflammatory properties in rats with liver fibrosis. J Hepatol. 2016;64:691–8.
74. Moore TL, Rodriguez-Lorenzo L, Hirsch V, Balog S, Urban D, Jud C, Rothen-Rutishauser B, Lattuada M, Petri-Fink A. Nanoparticle colloidal stability in cell culture media and impact on cellular interactions. Chem Soc Rev. 2015;44:6287–305.
75. Casals E, Gusta MF, Piella J, Casals G, Jimenez W, Puntes V. Intrinsic and extrinsic properties affecting innate immune responses to nanoparticles: the case of cerium oxide. Front Immunol. 2017;8:970.
76. Luan X, Sansanaphongpricha K, Myers I, Chen HW, Yuan HB, Sun DX. Engineering exosomes as refined biological nanoplatforms for drug delivery. Acta Pharmacol Sin. 2017;38:754–63.
77. Sen S, Xavier J, Kumar N, Ahmad MZ, Ranjan OP. Exosomes as natural nanocarrier-based drug delivery system: recent insights and future perspectives. 3 Biotech. 2023;13.
78. Chen JX, Huang XY, Wang P, Lin WT, Xu WX, Zeng M. Effects and mechanism of arachidonic acid against TNF-alpha induced apoptosis of endothelial cells. Clin Hemorheol Microcirc. 2021;77:259–65.
79. Jiang S, Wang ZG, Riethoven JJ, Xia YN, Miner J, Fromm M. Conjugated Linoleic acid activates AMP-Activated protein kinase and reduces adiposity more effectively when used with Metformin in mice. J Nutr. 2009;139:2244–51.
80. Yang B, Zhou Y, Wu MJ, Li XS, Mai KS, Ai QH. ω-6 polyunsaturated fatty acids (linoleic acid) activate both autophagy and antioxidation in a synergistic feedback loop via TOR-dependent and TOR-independent signaling pathways. Cell Death Dis. 2020;11.
81. Tong XS, Ganta RR, Liu ZP. AMP-activated protein kinase (AMPK) regulates autophagy, inflammation and immunity and contributes to osteoclast differentiation and functionabs. Biol Cell. 2020;112:251–64.
82. Heckert EG, Seal S, Self WT. Fenton-like reaction catalyzed by the rare Earth inner transition metal cerium. Environ Sci Technol. 2008;42:5014–9.
83. Baldim V, Bedioui F, Mignet N, Margaill I, Berret JF. The enzyme-like catalytic activity of cerium oxide nanoparticles and its dependency on Ce surface area concentration. Nanoscale. 2018;10:6971–80.

Publisher's note